



저작자표시 2.0 대한민국

이용자는 아래의 조건을 따르는 경우에 한하여 자유롭게

- 이 저작물을 복제, 배포, 전송, 전시, 공연 및 방송할 수 있습니다.
- 이차적 저작물을 작성할 수 있습니다.
- 이 저작물을 영리 목적으로 이용할 수 있습니다.

다음과 같은 조건을 따라야 합니다:



저작자표시. 귀하는 원저작자를 표시하여야 합니다.

- 귀하는, 이 저작물의 재이용이나 배포의 경우, 이 저작물에 적용된 이용허락조건을 명확하게 나타내어야 합니다.
- 저작권자로부터 별도의 허가를 받으면 이러한 조건들은 적용되지 않습니다.

저작권법에 따른 이용자의 권리는 위의 내용에 의하여 영향을 받지 않습니다.

이것은 [이용허락규약\(Legal Code\)](#)을 이해하기 쉽게 요약한 것입니다.

[Disclaimer](#) 

공학박사 학위논문

**Analysis of Operational Reliability of
Organic Field Effect Transistors and its
Application**

유기 트랜지스터의 안정성에 관한 연구 및 그 응용

2013 년 8 월

서울대학교 대학원

재료공학부

장준혁

Analysis of Operational Reliability of Organic Field Effect Transistors and its Application

지도 교수 김 장 주

이 논문을 공학박사 학위논문으로 제출함

2013 년 8 월

서울대학교 대학원

재료공학부

장 준 혁

장준혁의 공학박사 학위논문을 인준함

2013 년 8 월

위 원 장 _____ 박 수 영

부위원장 _____ 김 장 주

위 원 _____ 서 용 석

위 원 _____ 김 기 범

위 원 _____ 노 용 영



(인)



(인)



(인)

Abstract

Analysis of Operational Reliability of Organic Field Effect Transistors and its Application

Junhyuk Jang

Department of Materials Science and Engineering

The Graduate School

Seoul National University

The operational reliability is one of the most important parameters to evaluate the performance of organic field effect transistors. To analyze operational stability, in this thesis, a defined continuous or alternating voltage signal is applied to the gate, source, and drain electrodes for a period of time, and the FET characteristics is monitored periodically as a function of time in a controlled environment.

Chapter 1 describes the basic theory of a semiconductor and a field effect transistor. Organic materials for FETs and application of OFETs are also introduced.

In the chapter 2, air stable n-type organic field effect transistors based on C₆₀ are realized using a perfluoropolymer as the gate dielectric layer. The devices showed the field-effect mobility of 0.049 cm²/V•s in ambient air. Replacing the gate dielectric material by SiO₂ resulted in no transistor action in ambient air. Perfluorinated gate dielectric layer reduces interface traps significantly for the n-type semiconductor even in air.

Application of the stable OFETs to ion and bio sensor is described in chapter 3. The operational stability of OFET is the most important factor to have success of these sensors due to their working environment such as aqueous media. The proton sensitive sensor fabricated with ion-detective dielectric passivation layer. The current change with different pH buffer solution was analyzed. Bovine serum albumin was covalently attached to a modified surface to selectively detect the label free monoclonal antiBSA. These sensors displayed a high affinity constant (KA) of (1.1x10⁷ M⁻¹ at pH 7, which is 1 order of magnitude higher than those obtained with a highly sensitive surface plasmon resonance spectroscopy detection system. This demonstration of fast, label-free, real-time detection of nanoscale

biomolecules in aqueous buffer solutions using the organic transistor sensing platform will have a significant impact on high performance microarrays in addition to discriminating the presence of ionizable groups.

In the chapter 4, n-type P(NDI2OD-T2) polymer semiconductor used as n-type OFET and investigate the relationship between concentration of dopant and electrical characteristics. The field-mobility mobility of highly-crystalline CsF doped OFET devices are not affected by doping concentration. But the field-mobility and the bias stress resistance of amorphous C₆₀ doped OFET devices are increased to 0.72 cm²/V•sec from 0.35 cm²/V•sec and threshold voltage is decreased to 3.2 V from 8.6 V. Microstructure analysis with synchrotron X-ray diffraction geometries was followed. These improvements are due to trap-filling with excess charge from dopants and enhanced microstructural arrangement attributed to charge-transfer complexes between dopant molecule and host polymer

Keywords: organic semiconductor, doping, organic field effect transistor, bio-sensor, mobility, stability

Student Number: 2004-23463

Contents

Abstract	ii
Contents	v
List of Tables.....	ix
List of Figures	x
1 . Introduction	1
1.1 The Semiconductors.....	1
1.2 Bands and Band Bending	3
1.3 The Field Effect Transistor.....	7
1.3.1 Gradual Channel Approximation	9
1.3.2 Electrical Characteristics.....	13
1.4 Materials for Organic Field Effect Transistors	14
1.5 Application of OFETs	21
1.5.1 Electrophoretic Displays	21
1.5.2 OFET-Driven Flexible OLED Displays.....	24
1.5.3 Organic Integrated Circuits	27

1.6	Outline of thesis	29
1.7	Bibliography	30
2	. Air stable n-type Organic Field Effect Transistors with a perfluoro-polymer as insulation and passivation layer	38
2.1	Introduction	38
2.2	Experimental.....	40
2.3	Result and Discussion	43
2.3.1	FET characteristics	43
2.3.2	Stability characteristics	46
2.3.3	CYTOP passivation layer for pentacene OFET devices...51	
2.3.4	CYTOP passivation layer for IGZO FET devices.....54	
2.4	Conclusion.....	61
2.5	Bibliography	62
3	. In Situ Antibody Detection Using Aqueous Stable Pentacene Transistor Biosensors	64

3.1	Introduction	64
3.2	Experimental.....	67
3.3	Result and Discussion	70
3.3.1	FET characteristics in aqueous media	70
3.3.2	Chemical responsivity.....	76
3.3.3	Antibody detection	78
3.4	Conclusion.....	90
3.5	Bibliography	91

4 . Effect of n-type doping to Organic Field Effect

Transistors94

4.1	Introduction	94
4.2	Experiment	100
4.3	Result and Discussion	103
4.3.1	FET characteristics of doped polymer	103
4.3.2	Stability of electrical parameter	111
4.3.3	Crystallinity analysis with X-ray scattering	115

4.4	Conclusion.....	119
4.5	Bibliography	120
초	록.....	124
List of publications	126

List of Tables

- Table 3.1** Electrical parameter difference in working environment.....73
- Table 4.1** Summary of electrical property of OFET based on the
pristine P(NDI2OD-T2) with different doping ratio 110

List of Figures

Figure 1.1	Band bending under (a) flat band conditions (no bias), (b) accumulation (negative bias), (c) depletion (positive bias), (d) inversion (large positive bias). The green dashed line indicates the Fermi level while the black dotted line indicates the midpoint of the bandgap	6
Figure 1.2	MOSFET (a) and OFET (b) schematic structures.....	12
Figure 1.3	Chemical structure of representative p-type organic semiconductor for FET	19
Figure 1.4	Chemical structure of representative n-type organic semiconductor for FET	20
Figure 1.5	(a) Flexible electronic-ink device (b) schematic structure of cross-sectional image of electronic-ink device	23
Figure 1.6	(a) Schematic image of cross-section of the top-emission OFET-driven OLED display. (b) Optical microscope image of a AMOLED pixel.....	26
Figure 1.7	Schematic image of inverter with (a) p-channel transistor and (b) n-channel transistor (c) The image of RFID tag with inkjet-printed OFET.....	28

Figure 2.1	Schematic illustration of C ₆₀ n-type OFET devices	42
Figure 2.2	Atomic Force Microscope Images on (a) SiO ₂ and (b) CYTOP surface (scan size : 1μm x 1μm).....	44
Figure 2.3	Output (I _D -V _D) characteristics of C ₆₀ OFETs with (a) SiO ₂ insulator in inert environment (passivated), (b) CYTOP insulator in ambient air, and (c) CYTOP insulator in inert environment (passivated).	45
Figure 2.4	Transfer (I _D -V _D) characteristics of C ₆₀ OFETs in saturation regime with (a) SiO ₂ insulator in inert environment (passivated), (b) CYTOP insulator in ambient air, and (c) CYTOP insulator in inert environment (passivated). Both forward scan (filled rectangle) and reverse scan (filled circle) are exhibited.	49
Figure 2.5	Time dependence of (a) mobility, (b) hysteresis, and (c) threshold voltage for forward and backward scan of encapsulated devices fabricated on SiO ₂ (circle), air exposed device on CYTOP (triangle) and encapsulated device on CYTOP TM (rectangle).	50
Figure 2.6	The transfer characteristics of pentacene OFET with/without CYTOP passivation.....	53

Figure 2.7 Transfer characteristics of a-IGZO FETs with CYTOP-passivation layer (solution process) and SiO _x -passivation layer (vacuum process) compared to unpassivated FET at $V_{DS} = 10$ V ($W/L = 100/20$ μm).	59
Figure 2.8 Threshold-voltage shift of a-IGZO FETs along with stress time under positive gate bias temperature stress ($V_{GS} = 20$ V and $V_{DS} = 0$ V for 5000 s at 30 °C)	60
Figure 3.1 Schematic structure of bio-sensitive OFET for anti-BSA detecting	69
Figure 3.2 (a) Transfer characteristics and (b) Output characteristics of OFET working in water	72
Figure 3.3 Changing of transfer characteristics as time passage with (a) non-optimized device (b) optimized device	74
Figure 3.4 Change of Mobility and threshold voltage shift as working condition.....	75
Figure 3.5 (a) The current response with various pH value (b) The transfer characteristic with various pH value	77
Figure 3.6 Charge discrimination experiments for BSA/antiBSA immunoassay formation in aqueous buffer solutions at different pHs using (a) OFET and (b) SPR sensors.....	87

Figure 3.7 Titration curves for BSA/antiBSA immunoassay formation using OFET and optical sensors. Solid arrows indicate the additions of antiBSA solutions and open arrows indicate the exchange with buffer solution. Red solid curves represent the Langmuir fits. OFET current response with exposure to antiBSA solutions at (a) pH 7 and (b) pH 5. SPR sensor titration with antiBSA solutions at (c) pH 7 and (d) pH 5.....88

Figure 3.8 The model for immunodetection using pentacene transistor sensors when antiBSA is diluted in buffer solution at (a) pH 5 and (b) pH 7.....89

Figure 4.1 Chemical structure of (a) P(NDI2OD-T2) (b) C₆₀ and (c) CYTOP99

Figure 4.2 Schematic illustration of Bottom contact/Top gate OFET device with n-type dopants..... 102

Figure 4.3 (a) The transfer characteristics of P(NDI2OD-T2) OFET in $V_D = 20\text{ V}, 80\text{ V}$ (b) Output characteristics of P(NDI2OD-T2) OFET with n-type operation 105

Figure 4.4 (a) Transfer characteristics of P(NDI2DO-T2) OFET with p-channel operation ($V_D = -20\text{ V}$) (b) Output characteristics

	of P(NDI2DO-T2) OFET with p-channel operation.....	106
Figure 4.5	(a) The transfer characteristics of OFETs with various amount of (a) Cocp ₂ and (b) CsF doping to P(NDI2OD-T2) semiconducting layer.	107
Figure 4.6	Output characteristics of P(NDI2DO-T2) OFET with (a) Cocp ₂ 0.5 wt% doping (b) CsF 0.5 wt% doping.....	108
Figure 4.7	(a) The mobility change with various amount of n-type doping (b) The threshold voltage change with various amount of n-type doping	109
Figure 4.8	A change of transfer characteristics after bias stress test with (a) pristine (b) Cocp ₂ doped (c) CsF doped devices.	113
Figure 4.9	The mobility change and threshold voltage shift with stress cycles.....	114
Figure 4.10	The in-plane x-ray diffraction patterns of the (a) P(NDI2OD-T2) with Cocp ₂ dopant (b) P(NDI2OD-T2) with CsF dopant.....	117
Figure 4.11	(a) The in-plane and (b) The out-of-plane x-ray diffraction patterns of pristine P(NDI2OD-T2) , Cocp ₂ and CsF film with wide range.....	118

1 . Introduction

1.1 The Semiconductors

A semiconductor is a solid whose electrical conductivity can be controlled over a wide range, either permanently or dynamically. Semiconductors have a well-defined bandgap between the valence and conduction bands and it is the size of the bandgap which determines many of the important semiconductor properties. A bandgap implies that rather than a continuum of possible energy states, there are some energies for which no corresponding electronic states exist. The density of states (DoS) is usually quoted in terms of energy; it is a measure of how many states exist at a given energy. Since electrons (and holes) are fermions they obey Fermi statistics, namely that

$$f(E, E_F) = \frac{1}{1 + \exp\left(\frac{E - E_F}{k_B T}\right)}$$

where k_B is the Boltzmann constant, T the temperature, E the energy and E_F the Fermi energy. For a semiconductor the Fermi-energy is normally found within the bandgap. The number of electrons and

holes in the semiconductor can be found by integrating the density of states with the Fermi occupation factor; however it is first necessary to determine the density of states. A frequently used approximation is to assume parabolic bands. This comes from assuming that all electrons are free which implies that the density of states varies as the square root of the energy.² In a disordered semiconductor, or one with defects, subbandgap states also exist, and these are often modeled either as an exponential tail (or double exponential tail) extending into the gap, or as a Gaussian distribution of states centered around some energy.

1.2 Bands and Band Bending

In inorganic semiconductors, the semiconductors usually are doped by the presence of dopant atoms. This shifts the Fermi level towards either the valence or conduction band, and so generates an imbalance of electrons or holes. The semiconductor is then said to be n-doped (electrons) or p-doped (holes).¹ Where two materials join, the Fermi levels will align. Close to the interface this will cause a local shift of the Fermi level relative to the band edges as holes (electrons) move to align the Fermi levels. If we have a p-n junction with p-doped semiconductor on one side and n-doped on the other, there will be a depletion zone with minimal carriers in between. The conventional way of visualising this is to consider that the bands bend close to the junction. Band bending also occurs in metal-insulator-semiconductor (MIS) diodes. Here, the band bending is due more to the potential bias between the metal and semiconductor than the work function, and so for clarity we will ignore work function effects in this discussion. The amount of bending can be calculated by solving the Poisson equation

$$\nabla^2 V = \frac{-\rho}{\epsilon}$$

where ρ is the charge density, and ϵ is the semiconductor permittivity. Applying a potential difference V between the semiconductor and the metal creates an offset of $-qV$ between the bulk Fermi energies. The majority of this potential difference will drop across the insulator however the displacement field must be continuous across the semiconductor-insulator interface. An electric field in the semiconductor is equivalent to a gradient in the band edge, but in the bulk semiconductor we have no electric field. The only way of reconciling these requirements is with band bending. How far into the semiconductor the bands bend depends on the density of states because a local potential V will shift the apparent Fermi level by qV and hence alter the hole and electron densities. It is then possible to solve the Poisson equation and extract the precise band shape.

Figure 1.1 (a) shows the band profile for a p-doped semiconductor under a variety of bias conditions. Under a negative bias (b) the bands will bend upwards. This will cause an accumulation of holes at the interface; this situation is termed "accumulation". If a positive bias is applied, the bands will bend the other way. For moderate positive biases the effect is to deplete the semiconductor of holes close to the interface (c); however when the Fermi level crosses the midpoint of the

bandgap a situation termed "inversion" occurs (d). Close to the interface a thin layer of electrons (the minority carrier in a p-doped material) is induced. Further increases in the bias will increase this electron concentration

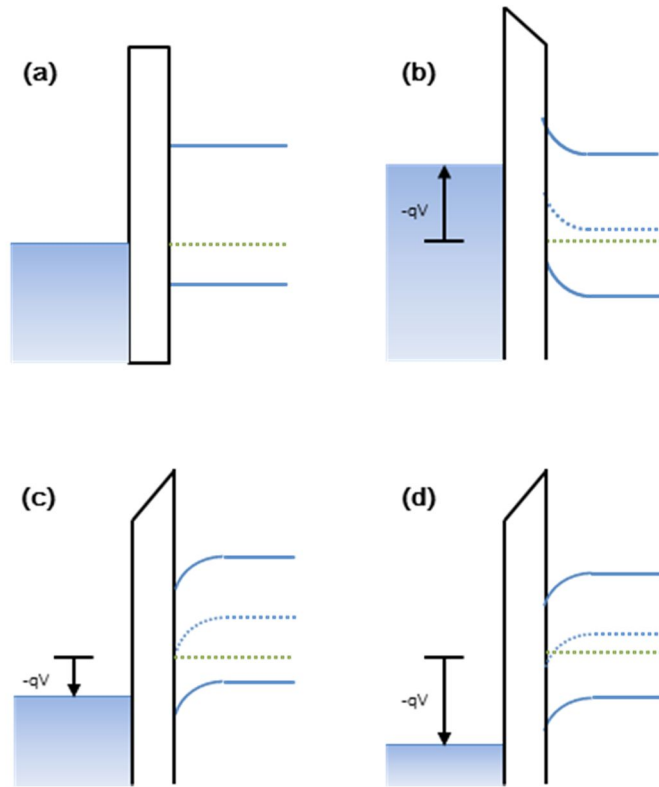


Figure 1.1 Band bending under (a) flat band conditions (no bias), (b) accumulation (negative bias), (c) depletion (positive bias), (d) inversion (large positive bias). The green dashed line indicates the Fermi level while the blue dotted line indicates the midpoint of the bandgap

1.3 The Field Effect Transistor

The transistor is arguably one of the most important inventions of the 20th century. It is easily one of the most prevalent inventions in the world, with many more transistors than people. The first documented working transistor (the Germanium point contact transistor) was created in 1947 at Bell Labs by Bardeen, Brattain and Shockley and they received the Nobel Prize in Physics in 1956 for this work. The name "transistor" was coined by John Pierce via an employee ballot at Bell Labs. Shockley developed the bipolar junction transistor in 1950 and it was this device which enabled the transistor radio. The transistors used in this thesis are instead based on the metal-oxide-semiconductor field-effect transistor (MOSFET) device structure which was invented in 1960 by Kahng and Atalla, again at Bell Labs. Silicon MOSFETs have a thin layer of oxide sandwiched between a metal gate and alightly doped semiconductor. This is the MIS structure discussed above. The MOSFET has an additional two contacts (source and drain) on the semiconductor with an opposite dopant to that of the semiconductor bulk. The two p-n junctions block any current flow

between the source and drain. However, if the gate bias causes inversion to occur in the lightly doped semiconductor region then current can flow and the transistor switches on.

1.3.1 Gradual Channel Approximation

Field effect transistors, an increase in the gate voltage will increase the number of carriers and hence increase the current flowing from source to drain. To calculate the current flow, one has to simultaneously solve the Poisson equation and the drift diffusion current equation

$$J_h = qp\mu_h E - qD_h \frac{dp}{dx}$$

(where μ_h is the hole mobility, q the electronic charge, E the electric field, D_h the diffusion constant for holes, and x the distance coordinate) in three dimensions. This is not trivial. However, several approximations dramatically reduce the complexity. The first is to reduce the number of dimensions to two by ignoring any effects from the edges of the device. In other words, the structures shown in Figure 1.2 have a width W which can be assumed to extend infinitely into the page. The second vital approximation is the gradual channel approximation.¹ This says that the electric field across the dielectric insulator will be significantly greater than the electric field between source and drain. This allows us to decouple the two two dimensional equations into two separate one-dimensional equations. The charge density is found by applying the one-dimensional Poisson equation

across the insulator, and then the current is found by applying the one-dimensional current equation between source and drain. The result of applying a voltage V_g to the gate is to induce a charge density of $C_i V_g$ in the semiconductor layer, where C_i is the capacitance per unit area of the dielectric. If instead of setting the semiconductor potential, $V(x)$, to zero everywhere we let it vary with position, then at position x there will be a charge density of $C_i(V_g - V(x))$. The electric field $E = -dV/dx$ and so the current at position x is given by

$$I = W\mu C_i(V_g - V(x)) \frac{dV}{dx}$$

We can integrate this from $x = 0$ to $x = L$, since $V(x = 0) = V_s = 0$ and $V(x = L) = V_d$ (ignoring contact resistance). This gives

$$I = \frac{W}{L} \mu C_i (V_g V_d - \frac{1}{2} V_g^2)$$

For $V_d \ll V_g$ we can neglect the quadratic term in V_d and we have the linear field effect transistor equation of

$$I = \frac{W}{L} \mu C_i V_g V_d$$

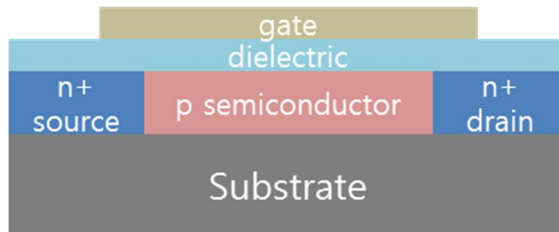
When the drain voltage is greater than the gate voltage there will be a region of the channel where no charges are accumulated. This is sometimes termed channel pinch off. As a result of this, the drain current supported by the transistor saturates with no further increases

seen for an increase in drain potential. The current is then given by

$$I = \frac{W}{L} \mu C_i V_g^2$$

and the transistor is said to be in saturation.

(a)



(b)

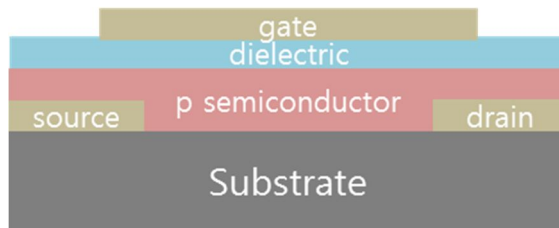


Figure 1.2 Schematic structures of (a) MOSFET and (b) OFET

1.3.2 Electrical Characteristics

Transistors are normally measured by taking transfer and output sweeps. A transfer sweep involves holding the drain voltage constant and sweeping the gate voltage. Generally both a linear (small drain voltage) and saturated (large drain voltage) sweep are performed. An output sweep involves holding the gate voltage constant and sweeping the drain voltage. To calculate the linear mobility, the gradient of a graph of I vs V_g is taken, while the saturated mobility is calculated from the gradient of I vs V_g . However, often the intercept of the line occurs at some non-zero V_g . This is due to trapped charge and the transistor equations can be modified to account for this, becoming

$$I = \frac{W}{L} \mu C_i (V_g - V_T) V_d$$

$$I = \frac{W}{L} \mu C_i (V_g - V_T)^2$$

The quantity V_T is called the threshold voltage. While to some extent V_T is just a fitting parameter, it corresponds to the point at which the majority of the deep traps are filled and meaningful transport occurs. This is not the same as the switch-on voltage (V_{on}) for the device, which is the point at which the current increases rapidly with increasing gate voltage.

1.4 Materials for Organic Field Effect Transistors

Currently, the performance of OFETs is surpassing that of amorphous silicon (a-Si) FETs with field-effect mobilities of 0.1–1 $\text{cm}^2/\text{V}\cdot\text{s}$ and on/off ratios of 10^6 – 10^8 , and is approaching that of poly crystalline silicon (c-Si) FETs ($>10 \text{ cm}^2/\text{V}\cdot\text{s}$). The state-of-the-art charge carrier mobilities for thin film OFETs are 17.2 $\text{cm}^2/\text{V}\cdot\text{s}$ in the case of vacuum-deposited small molecules,³ 31.3 $\text{cm}^2/\text{V}\cdot\text{s}$ for solution-processed small molecules,⁴ and 10.5 $\text{cm}^2/\text{V}\cdot\text{s}$ for conjugated polymers.⁵ For bulk single crystal devices, mobility as high as 15–40 $\text{cm}^2/\text{V}\cdot\text{s}$ has been reported.^{6–9}

Vacuum-deposited OFETs have been extensively investigated. Various π -conjugated oligomers (e.g., oligothiophenes^{10,11}) and macrocyclic compounds (e.g., copper phthalocyanines, CuPc¹²) were synthesized and tested.¹³ Pentacene is one of the first OSCs that showed record mobility values initially greater than 0.1 $\text{cm}^2/\text{V}\cdot\text{s}$ on SiO_2/Si substrates,¹⁴ subsequently reaching 1.5 $\text{cm}^2/\text{V}\cdot\text{s}$ on chemically modified SiO_2/Si substrates, and then 3–6 $\text{cm}^2/\text{V}\cdot\text{s}$ on polymer gate

dielectrics.^{16,17~19} Later, when a pentacene quinone was used to modify the dielectric surface, a record mobility of 35 cm²/V•s was reported.²⁰ Even though pentacene based OFETs have been incorporated into some prototype electronic devices,²¹⁻²³ their commercialization is still largely hindered because of the difficulty associated with pentacene purification, as well as poor device storage and operation stability. Therefore, a large number of small molecule organic semiconductors have been designed and prepared, leading to mobilities higher than 1.0 cm²/V•s and ranging from linear acenes to tetrathiafulvalene derivatives, coronene derivatives and metal phthalocyanines.²⁴ Currently, the state-of-art vacuum deposited-OFETs based on alkylated dinaphtho[2,3-b:2',3'-f]thieno[3,2-b]thiophenes (Cn-DNTTs) have reached thin film mobility close to 8.0 cm²/V•s and a high on/off ratio of 10⁸, with good environmental storage stability.²⁵

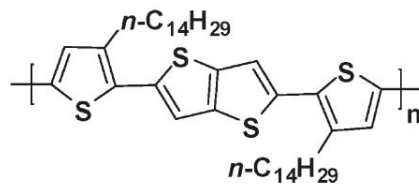
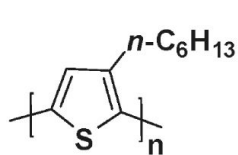
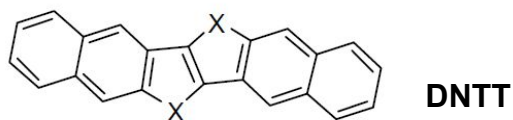
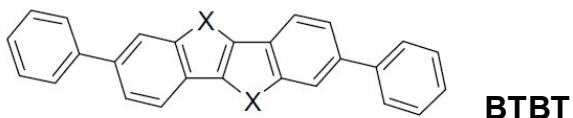
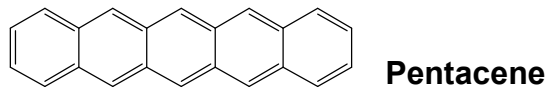
Vacuum deposition is a useful technique to deposit OSC thin films for OFETs. However, this approach is not amenable to low-cost and fast production. Solution processing is of great interest because it is compatible with the widely used high throughput printing techniques and can potentially lead to low cost fabrication. In this regard, solution-

processed OFETs have received a great deal of attention. Solution-processed OFETs can be divided into two categories based on the active materials, namely small molecule and polymer based OFETs. Solution-processed OFETs based on soluble oligothiophenes, substituted acenes and alkylated macrocyclic compounds have been subjected to extensive investigation.^{24,26-34} Other types of solution-processed OFETs are processed through soluble precursors, in which actual functional OSCs are generated in the later stage via thermal treatment or photoirradiation.³⁵⁻³⁸ This method has been often used in linear acenes.^{14,39,40} The performance of solution-processed OFETs and vacuum-deposited OFETs based on the same molecule, however, can be drastically different. In other words, processing conditions play a critical role in charge transport properties. Currently, there are only a few solution-processable small molecule OSCs with charge mobilities over $1.0 \text{ cm}^2/\text{V}\cdot\text{s}$.^{29,41,42} The most notable example is 6,13-bis(triisopropylsilylethynyl) pentacene (TIPS-PEN), which has recently displayed a mobility of $4.6 \text{ cm}^2/\text{V}\cdot\text{s}$ by tuning the molecular packing using a solution shearing process.⁴³ Benzothieno-[3,2-b][1]-benzothiophene (BTBT) derivatives constantly exhibit high FET

mobility.^{41,44}

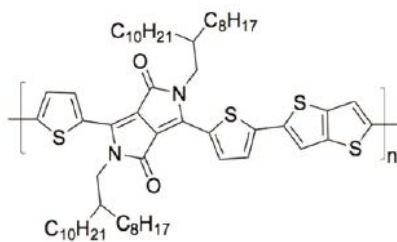
In the case of solution-processed polymer OFETs, regioregular poly(3-hexylthiophene) (P3HT) was the first polymer semiconductor that displayed high charge carrier mobility.⁴⁵⁻⁴⁷ However, P3HT suffers from poor environmental stability because of its relatively high oxidative potential. Subsequent tuning through reducing the number of side chains⁴⁸ and introducing fused ring systems (such as hieno-[3,2-b]thiophene polymer, PBTTT)⁴⁹ improved both stability and mobility. Notably, PBTTT gave charge-carrier field-effect mobilities of 0.2–0.6 $\text{cm}^2/\text{V}\cdot\text{s}$ and on/off ratios of 10^6 – 10^7 . More importantly, the performance of the polymers on exposure to low-humidity ($\sim 4\%$) air showed good operational stability with almost unnoticeable change of mobility, together with only a small positive threshold voltage shift and a slight decrease in the on/off ratio. Unfortunately, these devices still could not survive in ambient conditions (humidity level $\sim 50\%$). Moving from PBTTT to tetrathienoacene copolymers⁵⁰ and naphthodithiophene-based polymers,⁵¹ both performance and stability have been improved. More recently, donor–acceptor type polymers showed remarkable mobility, such as cyclopentadithiophene–

enzothiadiazole,⁵² diketopyrrolopyrrole^{5,53,54} and isoindigo⁵⁵⁻⁵⁷ based polymers. Charge carrier mobility values of OFETs have been pushed into the regime of c-Si FETs.^{5,55,58,59}



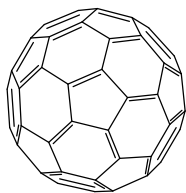
P3HT

PBTTT

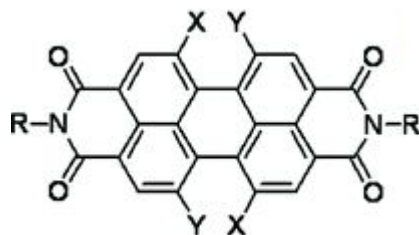


DPPT-TT

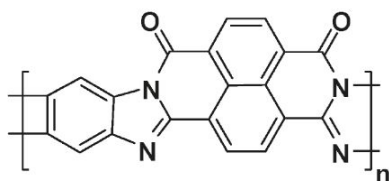
Figure 1.3 Chemical structure of representative p-type organic semiconductor for FET



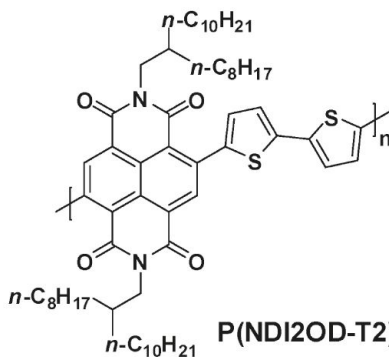
C₆₀



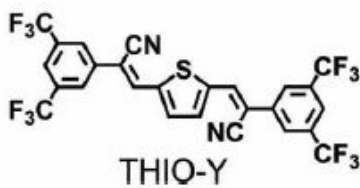
PTCDI



BBL



P(NDI2OD-T2)



THIO-Y

Figure 1.4 Chemical structure of representative n-type organic semiconductor for FET

1.5 Application of OFETs

1.5.1 Electrophoretic Displays

Flexible electrophoretic displays were recognized early on as an attractive first application of organic transistors.⁶⁰ This interest is driven by the desire for a display that has the readability and flexibility of paper, but with the capability to update the information on the page. In an electrophoretic display, charged sub-micrometer-sized pigment particles are suspended in a dielectric fluid that is enclosed into a sub-pixel-size cell or microcapsule. Different types of electrophoretic displays are being developed. In one mode, optical contrast is achieved by moving black and white sub-micrometer-sized pigment particles with opposite charge in a transparent fluid within a microcapsule.⁶¹ The polarity of the voltage determines which particle is presented to the viewer and thus sets the display color. In a variation on this theme, optical contrast is achieved by moving white particles in a colored fluid. When an electric field of one polarity is placed across the display panel, the particle moves towards the viewing side of the display, and the viewer sees the particle color. For the opposite polarity, the particles move to the rear of the display: the viewer sees the contrasting color of the fluid.⁶² Both single-particle and dual-

particle modes are capable of displaying grayscale through the partial movement of particles. The luminance and contrast of the dual-particle displays appears superior to single-particle displays in most cases. Typical switching takes hundreds of milliseconds, as a result of the low mobility of the particles within the fluid. More recently, Bridgestone developed a fast-response electrophoretic display⁶³ by suspending the particles in air, instead of liquid. However, the device requires high driving voltages. Electrophoretic displays have the inherent quality of being bright, even in sunlit conditions, due to the near-Lambertian scattering from the white particles used to form the image and the excellent absorption and low transparency of the black particles or colored oil. They are bistable. i.e., the image is maintained with no addition of power and requires external input (and power) only when the image needs to be changed, reducing power consumption. Finally, no polarizer films, alignment layers, rubbing processes, or spacers are needed. The result is a low-power, reflective display with a high brightness and paperlike contrast over all viewing angles, making electrophoretic materials ideal candidates for the use in flexible displays.

(a)



(b)

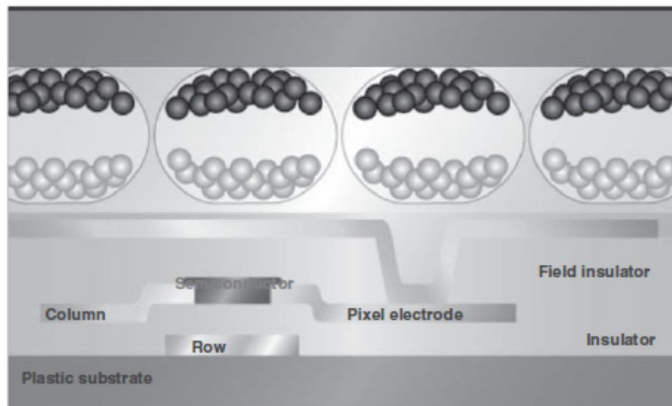


Figure 1.5 (a) Flexible electronic-ink device (b) schematic structure of cross-sectional image of electronic-ink device

1.5.2 OFET-Driven Flexible OLED Displays

OLEDs are suitable for flexible displays not only because they comprise of a thin, all-solid-state flexible structure, but also because their wide viewing angle allows them to be viewed even when they are flexed. Other advantages of OLEDs are their wide color gamut and quick response times, enabling full-color smooth-moving images even on flexible films. Thus OLED technology is a promising candidate for application in the front plane of high-quality flexible optical displays, the performance of which can be enhanced by the use of an active-matrix backplane. There have been several pioneering studies reporting green monochrome OFET-driven OLEDs (OFET-OLEDs) with bottom-emission structure. Chuman et al. first reported a green monochrome 8×8 pixels OLED display driven by pentacene OFETs on a glass substrate.⁶⁴ The patterning of a pentacene layer was done by shadow mask technique. Bottom-emission structure was employed for the integration of OLEDs and OFETs because of its simple integration architecture. Recently Suzuki et al. reported a full-color $213 \times \text{RGB} \times 120$ pixels OFET-OLED panel on a plastic substrate (polyethylene naphthalate, PEN).⁶⁵ Top-emission OLED displays have a more efficient structure for high-quality flexible displays due to a relative

small foot print of a pixel in contrast to a parallel-placed bottom-emission display. The employment of the top-emission OLED architecture contributed to not only high-resolution achievement but also a freedom to select the materials for OFET backplane and the plastic substrate to integrate the whole structure. Integration of top-emission OLEDs and OFETs requires elaborate integration architectures, in which OLEDs must be formed onto OFETs with suppressed degradation, which might be caused by multi-layer interdielectrics and interlayer-connections. This difficulty in the fabrication process has been a technological hurdle for the realization of AM top-emission OLEDs driven by OFETs. In this section, we present the materials, process, and device technologies that can be used to overcome this technological hurdle and achieve full color top-emission flexible OLED displays driven by an OFET backplane, fabricated onto a plastic substrate.⁶⁶

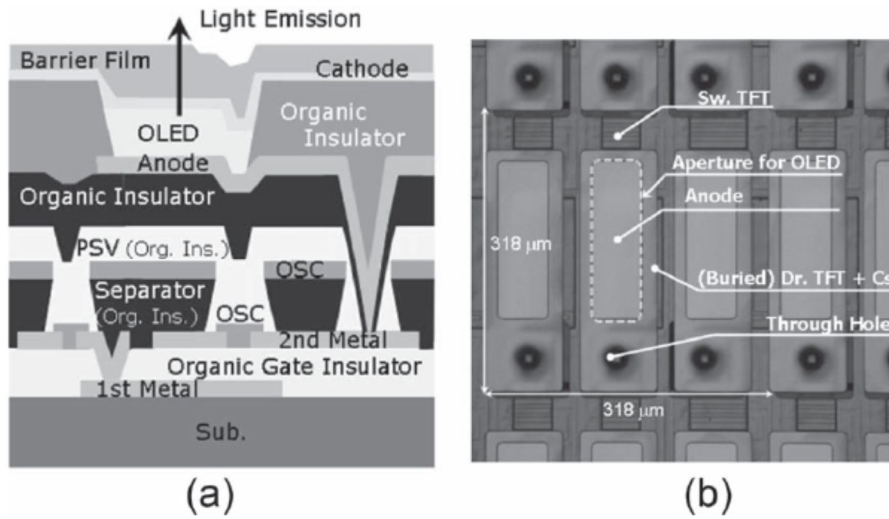


Figure 1.6 (a) Schematic image of cross-section of the top-emission OFET-driven OLED display. (b) Optical microscope image of a AMOLED pixel

1.5.3 Organic Integrated Circuits

Organic OFETs may also find application in microelectronic circuits that can be divided into two categories. The first category is digital circuits that are capable of processing digital information. An example is a transponder chip for an identification tag, where Boolean information from a memory is read out and prepared for radio frequency (RF) transmission to a base station. The second type of circuits are so-called analog circuits, typically used for conditioning, filtering, and amplifying analog signals, or for conversion of analog signals into a stream of Boolean digits.

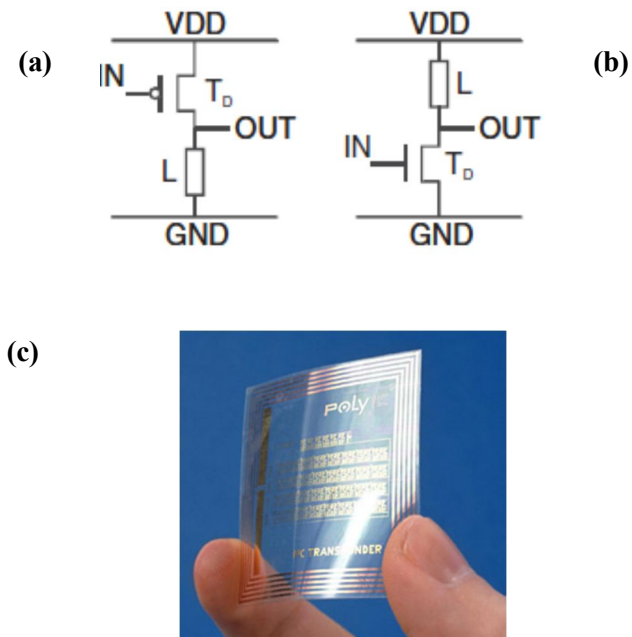


Figure 1.7 Schematic image of inverter with (a) p-channel transistor and (b) n-channel transistor (c) The image of RFID tag with inkjet-printed OFET

1.6 Outline of thesis

This thesis investigates the electrical characteristics of Organic Field Effect Transistors and its application.

The air stability of n-type organic field effect transistors was investigated by focusing to role of interface between dielectric insulator and semiconducting layer. The performance of Hydroxyl-free fluorinated polymer as insulating layer and passivation layer was compared with SiO₂ layer (CHAPTER 2).

The Organic Field Effect Transistor was used as In-situ antibody detection. Bovine serum albumin was covalently attached to the transistor surface to selectively detect the label free monoclonal antiBSA. The sensitivity was compared with conventional sensing technique, surface plasmon resonance (SPR) spectroscopy (CHAPTER 3).

The Effect of doping to polymeric semiconductor was studied as kind and concentration of dopant. Electrical characteristics and reliability of doped Organic Field Effect Transistors were analysed. X-ray Diffraction studies revealed the crystallinity of polymeric semiconductor after doping (CHAPTER 4).

1.7 Bibliography

1. S. M. Sze., Physics of Semiconductor Devices., JohnWiley and Sons, 2nd edition (1981)
2. N. W. Ashcroft and N. D. Mermin, Solid State Physics. Brooks Cole, 1st edition, 1976.
3. Amin, A. Y.; Khassanov, A.; Reuter, K.; Meyer-Friedrichsen, T.; Halik, M. J. Am. Chem. Soc **134**, 1654 (2012)
4. Minemawari, H.; Yamada, T.; Matsui, H.; Tsutsumi, J. y.; Haas, S.; Chiba, R.; Kumai, R.; Hasegawa, T. Nature, **475**, 364 (2011)
5. Li, J.; Zhao, Y.; Tan, H. S.; Guo, Y.; Di, C.-A.; Yu, G.; Liu, Y.; Lin,M.; Lim, S. H.; Zhou, Y.; Su, H.; Ong, B. S. Sci. Rep. **2**, 754 (2012)
6. Menard, E.; Podzorov, V.; Hur, S. H.; Gaur, A.; Gershenson, M.E.; Rogers, J. A. Adv. Mater. , **16**, 2097 (2004)
7. Jurchescu, O. D.; Popinciuc, M.; van Wees, B. J.; Palstra, T. T. M. Adv. Mater., **19**, 688(2007)
8. Reese, C.; Bao, Z. Adv. Mater., **19**, 4535 (2007)
9. Sundar, V. C.; Zaumseil, J.; Podzorov, V.; Menard, E.; Willett, R.L.; Someya, T.; Gershenson, M. E.; Rogers, J. A. Science, **303**,1644(2004).

10. Meng, H.; Zheng, J.; Lovinger, A. J.; Wang, B.-C.; Van Patten, P.G.; Bao, Z. *Chem. Mater.*, **15**, 1778(2003)
11. Mushrush, M.; Facchetti, A.; Lefenfeld, M.; Katz, H. E.; Marks, T. J. *J. Am. Chem. Soc.*, **125**, 9414(2003)
12. Bao, Z.; Lovinger, A. J.; Dodabalapur, A. *Appl. Phys. Lett.*, **69**, 3066(1996)
13. Liu, S.; Wang, W. M.; Briseno, A. L.; Mannsfeld, S. C. B.; Bao, Z. *Adv. Mater.*, **21**, 1217(2009)
14. Afzali, A.; Dimitrakopoulos, C. D.; Breen, T. L. *J. Am. Chem. Soc.*, **124**, 8812(2002)
15. Yen-Yi, L.; Gundlach, D. I.; Nelson, S. F.; Jackson, T. N. *IEEE Trans. Electron Devices*, **44**, 1325(1997).
16. M. E.; Senatore, M. L.; Zi, H.; Bao, Z. In *Organic Field-Effect Transistors*; Zhenan, B., Locklin, J. J., Eds.; CRC Press: Boca Raton, FL, p 159 (2007)
17. Yang, H.; Shin, T. J.; Ling, M.-M.; Cho, K.; Ryu, C. Y.; Bao, Z. *J. Am. Chem. Soc.*, **127**, 11542(2005)
18. Zhang, X.-H.; Tiwari, S. P.; Kim, S.-J.; Kippelen, B. *Appl. Phys. Lett.*, **95**, 223302(2009)

19. Roberts, M. E.; Mannsfeld, S. C. B.; Queraltó, N.; Reese, C.; Locklin, J.; Knoll, W.; Bao, Z. *Proc. Natl. Acad. Sci. U.S.A.*, **105**, 12134(2008)
20. Jurchescu, O. D.; Baas, J.; Palstra, T. T. M. *Appl. Phys. Lett.*, **84**, 3061(2004)
21. Kane, M. G.; Campi, J.; Hammond, M. S.; Cuomo, F. P.; Greening, B.; Sheraw, C. D.; Nichols, J. A.; Gundlach, D. J.; Huang, J.R.; Kuo, C. C.; Jia, L.; Klauk, H.; Jackson, T. N. *IEEE Electron Device Lett.*, **21**, 534(2000)
22. Gelinck, G. H.; Huitema, H. E. A.; van Veenendaal, E.; Cantatore, E.; Schrijnemakers, L.; van der Putten, J. B. P. H.; Geuns, T.C. T.; Beenhakkers, M.; Giesbers, J. B.; Huisman, B.-H.; Meijer, E. J.; Benito, E. M.; Touwslager, F. J.; Marsman, A. W.; van Rens, B. J. E.; de Leeuw, D. M. *Nat. Mater.*, **3**, 106(2004)
23. Rogers, J. A.; Bao, Z.; Baldwin, K.; Dodabalapur, A.; Crone, B.; Raju, V. R.; Kuck, V.; Katz, H.; Amundson, K.; Ewing, J.; Drzaic, P. *Proc. Natl. Acad. Sci. U.S.A.*, **98**, 4835(2001)
24. Wang, C.; Dong, H.; Hu, W.; Liu, Y.; Zhu, D. *Chem. Rev.*, **112**, 2208(2011)

25. Kang, M. J.; Doi, I.; Mori, H.; Miyazaki, E.; Takimiya, K.; Ikeda, M.; Kuwabara, H. *Adv. Mater.*, **23**, 1222(2011)
26. Kim, S. H.; Yoon, W. M.; Jang, M.; Yang, H.; Park, J.-J.; Park, C.E. *J. Mater. Chem.*, **22**, 7731(2012)
27. Feili, D.; Schuettler, M.; Doerge, T.; Kammer, S.; Stieglitz, T. *Sens. Actuators, A*, **120**, 101(2005)
28. Katz, H. E. *Chem. Mater.*, **16**, 4748(2004)
29. Zhang, L.; Di, C.-a.; Yu, G.; Liu, Y. *J. Mater. Chem.*, **20**, 7059 (2010)
30. Brown, A. R.; Jarrett, C. P.; de Leeuw, D. M.; Matters, M. *Synth. Met.*, **88**, 37(1997)
31. Payne, M. M.; Parkin, S. R.; Anthony, J. E.; Kuo, C.-C.; Jackson, T. *N. J. Am. Chem. Soc.*, **127**, 4986(2005)
32. Allard, S.; Forster, M.; Souharce, B.; Thiem, H.; Scherf, U. *Angew. Chem., Int. Ed.*, **47**, 4070 (2008).
33. Gao, P.; Beckmann, D.; Tsao, H. N.; Feng, X.; Enkelmann, V.; Baumgarten, M.; Pisula, W.; Müllen, K. *Adv. Mater.*, **21**, 213 (2009)
34. Gao, P.; Beckmann, D.; Tsao, H. N.; Feng, X.; Enkelmann, V.; Pisula, W.; Mullen, K. *Chem. Commun.*, 1548 (2008)

35. Garnier, F.; Hajlaoui, R.; El Kassmi, A.; Horowitz, G.; Laigre, L.; Porzio, W.; Armanini, M.; Provasoli, F. *Chem. Mater.*, **10**, 3334(1998)
36. Katz, H. E.; Lovinger, A. J. *Nature*, **404**, 478(2000)
37. Yamada, H.; Ohashi, C.; Aotake, T.; Katsuta, S.; Honsho, Y.; Kawano, H.; Okujima, T.; Uno, H.; Ono, N.; Seki, S.; Nakayama, K.-i. *Chem. Commun.*, **48**, 11136(2012)
38. Yamada, H.; Okujima, T.; Ono, N. *Chem. Commun.*, **0**, 2957 (2008)
39. Weidkamp, K. P.; Afzali, A.; Tromp, R. M.; Hamers, R. J. J. *Am. Chem. Soc.*, **126**, 12740 (2004)
40. Afzali, A.; Dimitrakopoulos, C. D.; Graham, T. O. *Adv. Mater.*, **15**, 2066(2003)
41. Ebata, H.; Izawa, T.; Miyazaki, E.; Takimiya, K.; Ikeda, M.; Kuwabara, H.; Yui, T. *J. Am. Chem. Soc.*, **129**, 15732(2007)
42. Mitsui, C.; Soeda, J.; Miwa, K.; Tsuji, H.; Takeya, J.; Nakamura, E. *J. Am. Chem. Soc.*, **134**, 5448(2012).
43. Giri, G.; Verploegen, E.; Mannsfeld, S. C. B.; Atahan-Evrenk, S.; Kim, D. H.; Lee, S. Y.; Becerril, H. A.; Aspuru-Guzik, A.; Toney, M. F.; Bao, Z. A. *Nature*, **480**, 504 (2011)

44. Uemura, T.; Hirose, Y.; Uno, M.; Takimiya, K.; Takeya, J. *Appl.Phys. Express*, **2**, 111501 (2009)
45. Bao, Z.; Dodabalapur, A.; Lovinger, A. J. *Appl. Phys. Lett.*, **69**, 4108(1996)
46. Sirringhaus, H.; Tessler, N.; Friend, R. H. *Science*, **280**,1741 (1998)
47. Wang, G.; Swensen, J.; Moses, D.; Heeger, A. J. *J. Appl. Phys.*, **93**, 6137(2003)
48. Ong, B. S.; Wu, Y.; Liu, P.; Gardner, S. J. *Am. Chem. Soc.*, , 3378 (2004).
49. McCulloch, I.; Heeney, M.; Bailey, C.; Genevicius, K.;MacDonald, I.; Shkunov, M.; Sparrowe, D.; Tierney, S.; Wagner, R.;Zhang, W.; Chabinye, M. L.; Kline, R. J.; McGehee, M. D.; Toney, M.F. *Nat. Mater.*, **5**, 328(2006)
50. Fong, H. H.; Pozdin, V. A.; Amassian, A.; Malliaras, G. G.;Smilgies, D.-M.; He, M.; Gasper, S.; Zhang, F.; Sorensen, M. J. *Am.Chem. Soc.*, **130**, 13202 (2008)
51. Osaka, I.; Shinamura, S.; Abe, T.; Takimiya, K. *J. Mater. Chem.C.*, 1297 (2013)

52. Tsao, H. N.; Cho, D. M.; Park, I.; Hansen, M. R.; Mavrinskiy, A.; Yoon, D. Y.; Graf, R.; Pisula, W.; Spiess, H. W.; Müllen, K. J. *Am.Chem. Soc.*, **133**, 2605(2011)
53. Sonar, P.; Singh, S. P.; Li, Y.; Soh, M. S.; Dodabalapur, A. *Adv.Mater.*, **22**, 5409(2010)
54. Nielsen, C. B.; Turbiez, M.; McCulloch, I. *Adv. Mater.* (2012)
55. Lei, T.; Cao, Y.; Fan, Y.; Liu, C.-J.; Yuan, S.-C.; Pei, J. J. *Am.Chem. Soc.*, **133**, 6099 (2011)
56. Lei, T.; Cao, Y.; Zhou, X.; Peng, Y.; Bian, J.; Pei, J. *Chem. Mater.*, **24**, 1762 (2012)
57. Mei, J.; Kim, D. H.; Ayzner, A. L.; Toney, M. F.; Bao, Z. J. *Am.Chem. Soc.*, **133**, 20130(2011)
58. Nielsen, C. B.; Turbiez, M.; McCulloch, I. *Adv. Mater.*, **25**,1859 (2013)
59. Lei, T.; Dou, J.-H.; Pei, J. *Adv. Mater.*, **24**, 6457 (2012)
60. J. A. Rogers , Z. Bao , K. Baldwin , A. Dodabalapur , B. Crone , V. R.Raju , V. Kuck , H. Katz , K. Amundson , J. Ewing , P. Drzaic , *Proc. Natl.Acad. Sci. USA.* , **98** , 4835 (2001)
61. B. Comiskey , J. D. Albert , H. Yoshizawa , J. Jacobson , *Nature* ,**394** , 253 (1998)

62. R. C. Liang , J. Hou , H. M. Zang , J. Chung , IDMC Dig. ,
351(2003)
63. R. Hattori , S. Yamada , Y. Masuda , N. Nihei , R. Sakurai , J. Soc.
Inf. Disp. , **12** , 405 (2004)
64. T. Chuman , S. Ohta , S. Miyaguchi , H. Satoh , T. Tanabe , Y.
Okuda , M. Tsuchida , Dig. Tech. Pap. – Soc. Inf. Disp. Int. Symp. ,
35 , 45 (2004)
65. M. Mizukami , N. Hirohata , T. Iseki , K. Ohtawara , T. Tada , S.
Yagyu , T. Abe , T. Suzuki , Y. Fujisaki , Y. Inoue , S. Tokito , T.
Kurita , IEEE Electron Device Lett., **27** , 249 (2006)
66. L. Zhou , A. Wanga , S.-C. Wu , J. Sun , S. Park , T. N. Jackson ,
Appl. Phys. Lett. , **88** , 083502 (2006)

2 . Air stable n-type Organic Field Effect Transistors with a perfluoro-polymer as insulation and passivation layer

2.1 Introduction

A large number of semiconducting organic and polymeric materials have been reported and high field effect mobilities with high on–off ratios have been realized.¹ Most of the materials are, however, p-type and fewer n-type materials have been reported up to now.^{2,3} Moreover most of the reported n-type organic semiconducting materials showed instability and sensitivity to air exposure. Moisture or hydroxyl- group at the interface has electron withdrawing characteristics and acts as trap sites in operation of n-type OFETs.^{4,5} Since acceptor-like trap states induce threshold voltage shift and destroy OFETs performance, in situ measurement in high vacuum chamber or device passivation techniques are employed to characterize n-type OFETs . Recently, hydroxyl-free gate dielectric such as divinyltetramethylsiloxane-bis(benzocyclobutene) derivative is reported to be able to yield n-

channel FET conduction in most conjugated polymers. However, it is also limited to the encapsulated devices.⁶ Two methods have been reported to overcome the problem. The first one is to use specially designed semiconductor materials with strong electron withdrawing groups.⁷⁻¹⁰ It helps to increase electron affinity and prevent reaction with moisture or oxygen in ambient air. Another one is to use large grain and highly packed polycrystalline semiconductor. It reduces permeation of moisture and oxygen into the active region of film.^{11,12}

In this thesis, I report another method to fabricate n-type OFETs stable in air without passivation, which is the use of a perfluorinated polymer as the gate dielectric layer. C₆₀ was employed as an n-type semiconductor, which is reported to be unstable upon exposure to ambient air if the device is fabricated on SiO₂ dielectric layer.¹³⁻¹⁵ I focused on the interface between semiconductor and insulator rather than semiconductor bulk itself. I selected CYTOPTM fluoropolymer as a dielectric insulator to reduce the effect of interface trap sites and fabricate ambient air-stable C₆₀ OFETs.

2.2 Experimental

OFET devices have a top-contact and bottom gate structure. The devices were fabricated on a heavily doped silicon wafer which works as the common gate electrode. Either thermally grown SiO₂(3000 Å) (device 1) or spin-coated CYTOPTM(3600 Å) (device 2) was used as the dielectric layer.

For the device 1, silicon dioxide layer was cleaned with H₂SO₄:H₂O₂ = 4:1 solution and rinsed with deionized water. The surface was treated with UV-O₃ for 10 min before the deposition of an organic semiconductor. For the device 2, CYTOPTM was purchased from Asahi Glass and spin-coated on a Si wafer. Native oxide of the Si wafer was removed using buffered oxide etchant before spin coating. 50 nm thick C₆₀ film was deposited onto the dielectric layers with thermal evaporation under a pressure of 2.0x10⁻⁶ torr. Deposition rate was 0.5 Å/s. Substrate temperature was maintained at 50°C and active region was patterned with a metal shadow mask. Au source and drain electrode were deposited by thermal evaporation under a pressure of 5.0 x10⁻⁷ torr with the deposition rate of 2.0 Å/s. The samples were

exposed to N₂ gas in a glove box to change the mask for the electrode deposition. Channel length and width were defined to 50 μm and 500 μm, respectively, with another metal shadow mask. Thickness of the electrodes was 1000 Å. Some fabricated devices were encapsulated with glass cans in a glove box. O₂ and H₂O levels in the globe box were under 1.0 ppm, respectively.

Electrical measurements were performed using an Agilent 4155C semiconductor parameter analyzer and a Suss PM8 probe station. All electrical measurements were performed in the dark. Atomic Force Microscope (AFM) topographic images were taken in a PSIA XE-100 scanning probe microscope with non-contact mode.



Figure 2.1 Schematic illustration of C₆₀ n-type OFET devices

2.3 Result and Discussion

2.3.1 FET characteristics

Figure.2.2 shows AFM images of the C₆₀ films on the insulators. The root-mean-square (RMS) roughness of the C₆₀ films are almost the same with 5.3 Å on CYTOPTM and 5.7 Å on SiO₂, respectively. The film grown on SiO₂ dielectric layer has almost the same grain size as the film grown on CYTOPTM layer, and these grains are not large enough to prevent permeation of oxygen or moisture through the grain boundaries, one of the methods to show stable FET characteristics in ambient air. Drain current–drain voltage (I_D–V_D) characteristics of C₆₀ based FETs with the SiO₂ and CYTOPTM insulator are displayed in Figure 2.3 for different gate biases (V_g). The device with the SiO₂ insulator exhibits n-type characteristics only when it was encapsulated (Figure 2.3(a)). The device without encapsulation does not show any transistor characteristics under exposure to air (not shown), which is consistent with the previous reports.^{13,14} In contrast, the device with the CYTOPTM insulator shows clear n-type I_D–V_D characteristics even in air without passivation (Figure 2.3(b)). If the device is encapsulated, the current was increased considerably (Figure 2.3(c)).

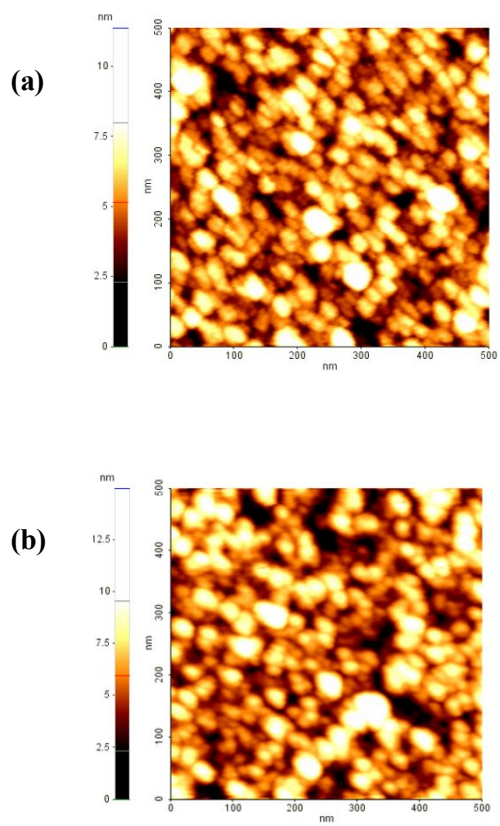


Figure 2.2 Atomic Force Microscope Images on (a) SiO₂ and (b) CYTOP surface (scan size : 1 μ m x 1 μ m)

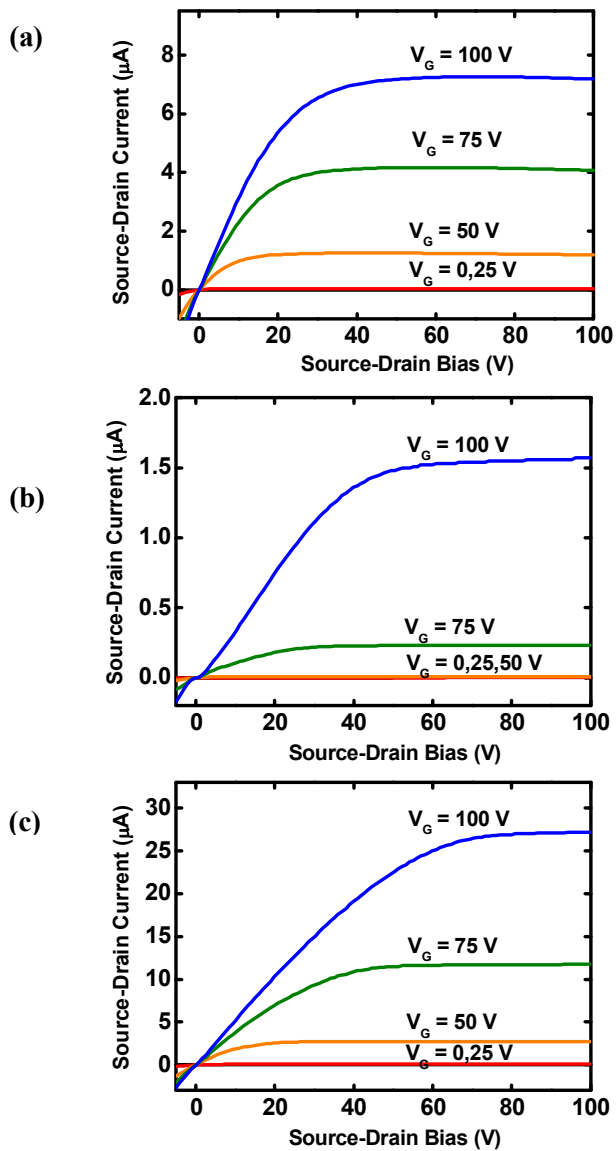


Figure 2.3 Output (I_D - V_D) characteristics of C_{60} OFETs with (a) SiO_2 insulator in inert environment (passivated), (b) CYTOP insulator in ambient air, and (c) CYTOP insulator in inert environment (passivated)

2.3.2 Stability characteristics

The transfer characteristics of the devices measured just after the fabrication of the devices ($t = 0$) in the saturation regime ($V_D = 100$ V) are shown in Figure 2.4. The device with SiO_2 gate dielectric layer (Figure 2.4 (a)) shows the electron mobility of $0.08 \text{ cm}^2/\text{V s}$, threshold voltage of 22.5 V, and on–off ratio of 10^4 , respectively. Moreover, the device showed large hysteresis of 42 V. In contrast to the device with SiO_2 insulator, the device with CYTOPTM insulator without encapsulation showed the electron mobility of $0.049 \text{ cm}^2/\text{V s}$ and on–off ratio of 6×10^3 in ambient air (Figure 2.4(b)), that is comparable with the encapsulated device with SiO_2 gate insulator. It is interesting to note that the device has very large threshold voltage of 64.0 V but with very small hysteresis. The encapsulated device with CYTOPTM gate insulator (Figure 2.3(c)) resulted in the best device performance as expected. The device showed the electron mobility of $0.20 \text{ cm}^2/\text{V s}$, threshold voltage of 29.0 V, and on–off ratio of 10^5 , respectively. To further evaluate the stability of the devices, I investigated the evolution of the transfer curves of the devices and the variation of mobility, threshold voltage and hysteresis with time are plotted in

Figure 2.5. Hysteresis in the figure was defined as the difference of gate bias between the forward and reverse scan at the source–drain current of 10 nA. The passivated device with SiO₂ insulator shows very large hysteresis of 42 V in the first scan. After the first scan, large threshold voltage shift more than 40 V was observed and hysteresis was reduced significantly to less than 5 V. Mobility was increased to 0.12 cm²/V•s at 100 s after the initial scan but slightly decreased after that point. This phenomenon can be understood by trap states at the interface between C₆₀ and silicon dioxide or in the thin transporting layer near the interface. As the gate bias increases in the first scan, the trap states are filled with electrons. These trapped electrons induce the hysteresis in the first scan and large threshold voltage shift from the second scan. After the originally empty deep traps are filled, charges are trapped only in shallow states. As results, the threshold characteristics do not change much and the mobility is increased. The device with CYTOPTM insulator in ambient air shows similar characteristics as the passivated device with SiO₂ insulator after the first scan. The device shows slowly decreasing mobility with time. The threshold voltage shift and hysteresis are maintained less than 5 V until 20,000 s. Almost similar threshold voltage of the unpassivated

device with CYTOPTM insulator and the passivated device with SiO₂ indicates that the trap density at the interface is almost the same between the two devices and the traps are filled by the exposure to the air in the CYTOPTM devices and by the first scan in the SiO₂ device. The source of decreasing mobility is understood by continuous generation of deep trap sites near the interface between the semiconductor and the insulators due to contact to ambient air including moisture and oxygen. The passivated device with the CYTOPTM insulator shows most stable characteristics without any significant change up to 2000 s after initial scanning. It had very low hysteresis (<2 V) and low threshold voltage shift (<2 V) up to that time. Higher electron mobility and lower threshold voltage of the encapsulated device than un-encapsulated device indicates that the trap density in the passivated device with CYTOPTM insulator is very low and the traps at the interface or thin transporting layer near the interface are generated by the exposure of the device to ambient air.

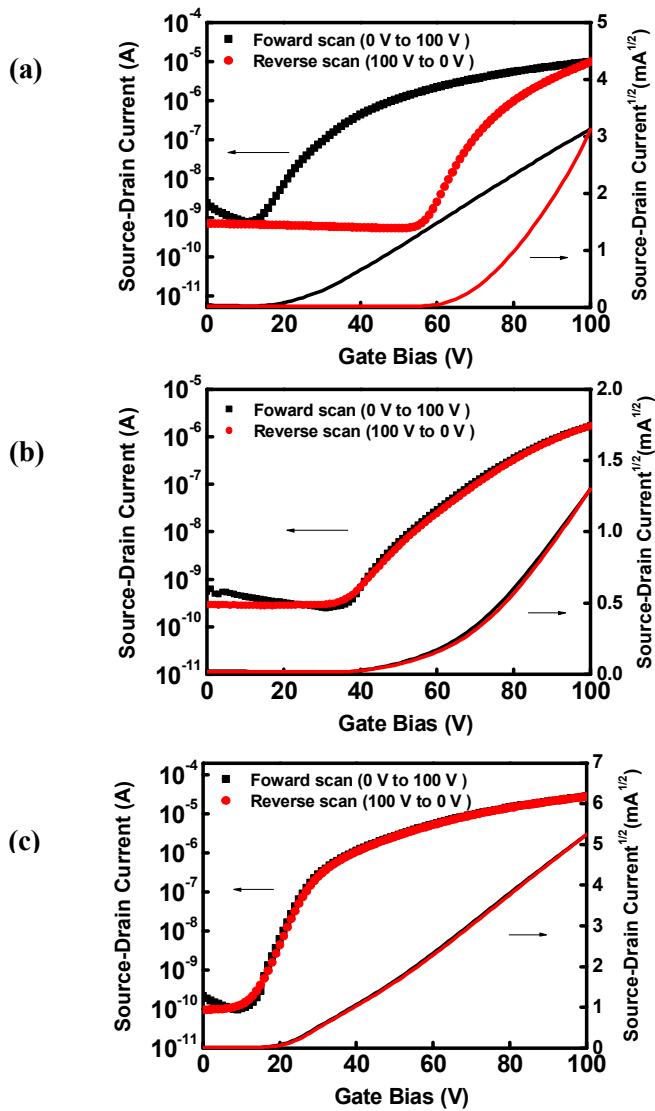


Figure 2.4 Transfer (I_D - V_D) characteristics of C_{60} OFETs in saturation regime with (a) SiO_2 insulator in inert environment (passivated), (b) CYTOP insulator in ambient air, and (c) CYTOP insulator in inert environment (passivated). Both forward scan (filled rectangle) and reverse scan (filled circle) are exhibited.

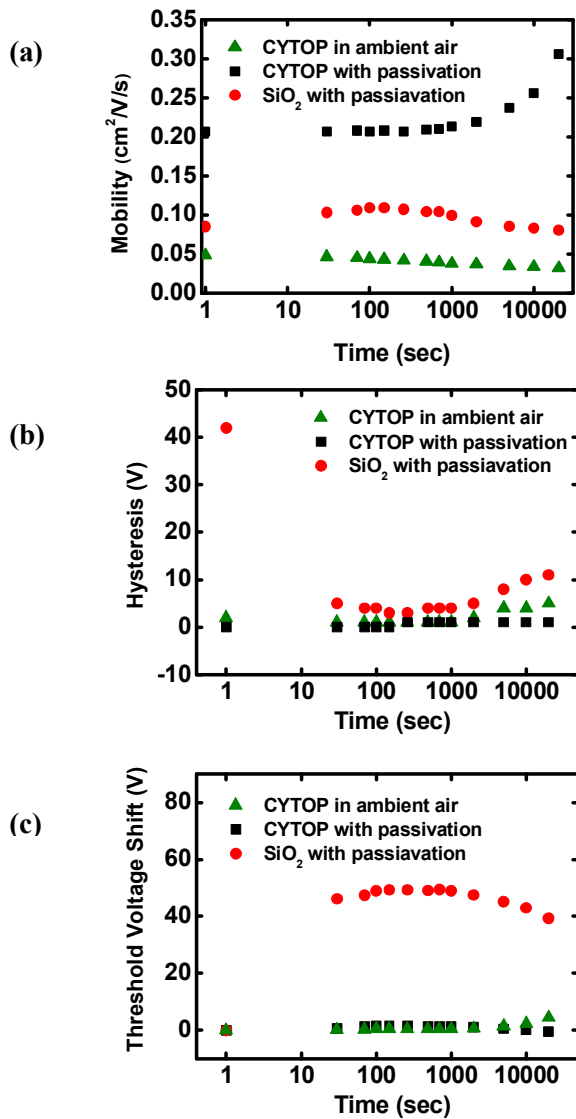


Figure 2.5 Time dependence of (a) mobility, (b) hysteresis, and (c) threshold voltage for forward and backward scan of encapsulated devices fabricated on SiO_2 (circle), air exposed device on CYTOP (triangle) and encapsulated device on CYTOPTM (rectangle).

2.3.3 CYTOP passivation layer for pentacene OFET

devices

The CYTOP polymer can be used as passivation layer due to low permeability of oxygen and moisture. The p-type Pentacene is selected for semiconducting material because of its high electrical performance and stability. Perfluorotrialkylamine, solvent of CYTOP, is orthogonal solvent for general organic molecule. The pentacene semiconducting layer was not damaged in spin-coating process of passivation deposition.

The transfer characteristics (I_D - V_G) of OFETs are displayed in figure 2.6. Blue and green scatters show forward and reverse scan of gate bias in ambient air without any passivation. Left axis is log scale of drain current and right axis is linear scale of square root of drain current. The mobility was $0.087 \text{ cm}^2/\text{V}\cdot\text{s}$ and threshold voltage was -6.5 V . Red and orange scatters show forward and reverse scan of gate bias with CYTOP passivation layer. The mobility and threshold voltage are slightly increased, $0.115 \text{ cm}^2/\text{V}\cdot\text{s}$ and -7.0 V . But hysteresis, difference of bias between forward and reverse direction scanning was decreased from 3.0 V to 0.5 V . I found OFET device with CYTOP

passivation works successfully without decreasing of performance. This passivation can be applied to another semiconducting material. Moreover, this passivation layer enables working OFET device in aqueous media. In the next chapter, detailed experiment and analysis can be described.

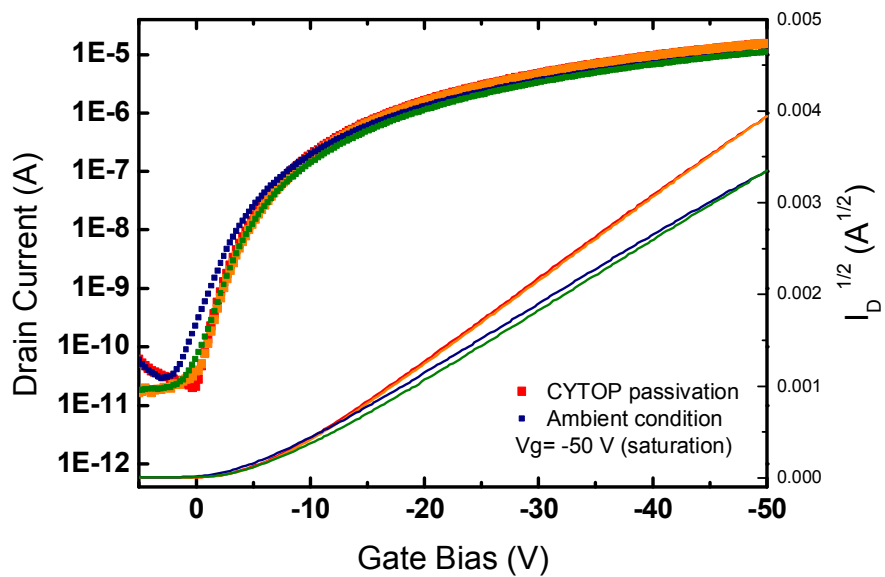


Figure 2.6 The transfer characteristics of pentacene OFET with/without CYTOP passivation

2.3.4 CYTOP passivation layer for IGZO FET devices

OFETs using indium–gallium–zinc-oxide (IGZO) semiconductors have attracted considerable attention for advanced displays due to characteristics such as light weight, large area, and flexible displays. Inorganic-passivation layers such as SiO₂ and SiN_x based on PECVD may cause degradation of electrical characteristics in IGZO FETs due to plasma-induced radiation damage to the back-channel region of FETs. The reliability of FETs passivated by polymer materials such as PVP and PMMA without plasma-induced damage is relatively poorer than that of FETs passivated by inorganic dielectric layers. It is well known that hydrogen and water, which can be reduced by employing a highly hydrophobic insulator, cause instability of amorphous IGZO (a-IGZO) FETs under gate bias stress. Therefore, the CYTOP passivation layer was used for improving the electrical characteristics and reliability of a-IGZO FETs, exploiting low annealing temperature (180°C). I successfully fabricated oxide FETs with solution-processed CYTOP passivation to avoid plasma damage and minimize environment-related reactions.

I fabricated CYTOP-passivated and SiO_x-passivated IGZO FETs.

The maximum process temperature of the SiO_x-passivation layer (200 nm thick) was 300 °C, whereas that of the CYTOP-passivation layer (240 nm thick) was not exceeding 180 °C.

I measured the initial transfer characteristics of a-IGZO FETs with the passivation layer consisting of SiO_x and CYTOP layers. These were compared to the one without a passivation layer in figure 2.7. Before measurements, all the FET samples used in this work were postannealed at 473 K (200 °C) for 2 h. This postannealing process could eliminate any processing damage during the FET fabrication process. The CYTOP-passivated device exhibits a better electric characteristic (saturation mobility (μ_{sat}) = 12.3 cm²/V · s and subthreshold swing (s-swing) = 0.35 V/dec) than the FET with the SiO₂-passivation layer (μ_{sat} = 5.8 cm²/V · s and s-swing = 0.57 V/dec) deposited by ICP-CVD. The saturation mobility of the CYTOP-passivated layer FET was even larger than that (6.4 cm²/V · s) of the unpassivated FET. The electrical characteristics of the a-IGZO semiconductor could easily be affected by the back surface of the IGZO channel layer. It has been previously reported that organic insulators having low polarity could provide a uniformly nonpolar and defect-free back-interface region by suppressing an interaction

between external environment and oxide surface (reversible shallow traps and irreversible defects). After CYTOP passivation, the hysteresis ($\Delta V_{TH} = 0.2$ V) was also remarkably reduced without degradation of the electrical characteristics compared to unpassivated FET ($\Delta V_{TH} = 0.8$ V). This can be attributed to the relatively low polarity of CYTOP, which constitutes a reduced dipolar (energetic) disorder at the IGZO/CYTOP interface region. However, the hysteresis phenomenon of the SiO_x-passivated FET ($\Delta V_{TH} = 2.5$ V) was seriously degraded due to plasma-induced damage to the back-channel region by ICP-CVD, which degraded the electrical characteristics of the IGZO FET.

In order to investigate the reliability of the CYTOP layer in oxide FETs under operating conditions. Threshold-voltage shift of a-IGZO FET along with stress time under PBTS (Positive gate Bias Temperature Stress, $V_G = 20$ V and $V_{DS} = 0$ V for 5000 s at 30°C) with gate and drain bias $V_G = 20$ V and $V_{DS} = 0$ V on the a-IGZO FET at 30°C for 5000 s. It is widely known that oxide FET with organic-passivation layer exhibits a larger V_{TH} shift compared to unpassivated FET due to O₂ adsorption and H₂O desorption under the PBTS

condition. The figure 2.8 demonstrates the threshold-voltage shift of IGZO FETs ($W/L = 100/20 \mu\text{m}$) under PBTS with stress time. The variation in the threshold voltage (ΔV_{TH}) of the FET with the SiO_x- and the CYTOPTM passivation layer was 3.3 and 2.8 V under identical bias conditions, respectively. The threshold-voltage shift (ΔV_{TH}) of the FET with the CYTOP-passivation layer was smaller with respect to the bias-temperature stress compared to the other FETs, including the 4.5-V V_{TH} shift of the unpassivated device with no change in mobility and s-swing. The difference in the threshold-voltage shifts among the three devices under PBTS ($V_{\text{G}} = 20 \text{ V}$ and $V_{\text{DS}} = 0 \text{ V}$ for 5000 s at 30°C) might be due to differences in the insulation property of the passivation layer, which prevents external environmental effects from ambient atmosphere.

In particular, for the SiO_x passivated FET, plasma-induced damage to the IGZO active layer appears to affect the reliability of oxide FET. The V_{TH} instability of IGZO FETs under bias-temperature stress is closely related to ambient effects such as the chemical reaction between the back-channel region and the ambient oxygen/water vapor. Chemical adsorption of oxygen and desorption of water vapor near the

back interface of the channel region, which might be encouraged by the bias-temperature stress condition, may facilitate V_{TH} instability. Because there is no defect site (oxygen vacancy) generated by plasma damage in the IGZO back-channel region, there might be relatively little interaction between IGZO back-channel/CYTOPTM passivation layers.

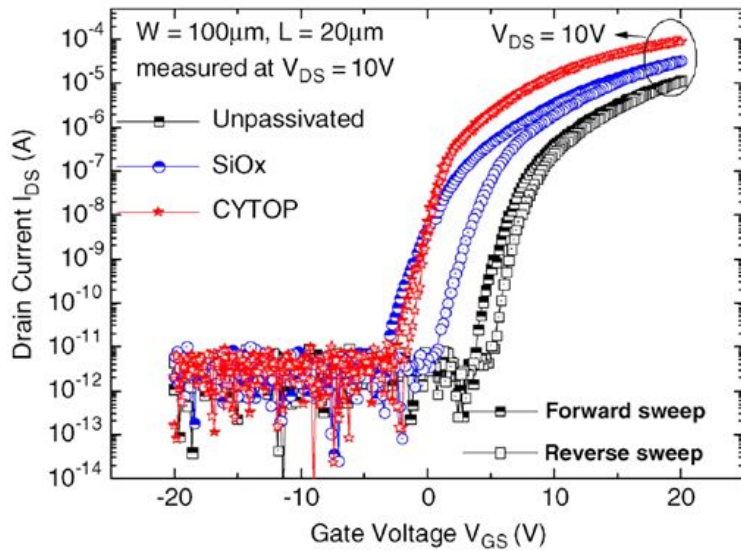


Figure 2.7 Transfer characteristics of a-IGZO FETs with CYTOP-passivation layer (solution process) and SiOx-passivation layer (vacuum process) compared to unpassivated FET at $V_{DS} = 10$ V ($W/L = 100/20 \mu\text{m}$).

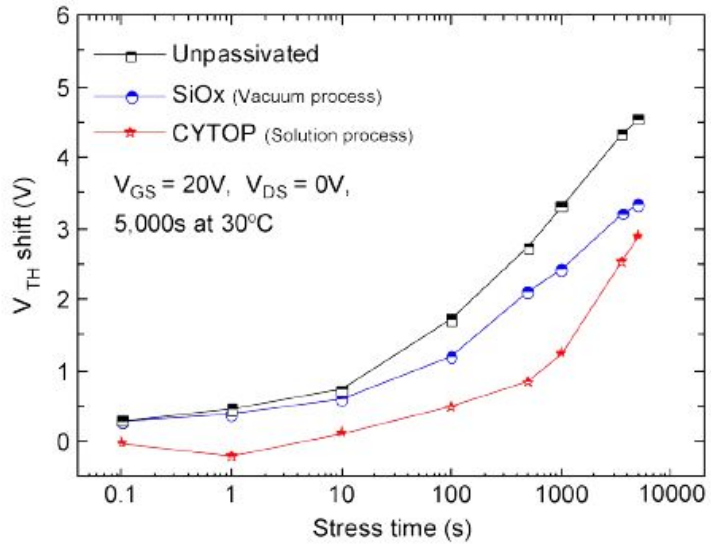


Figure 2.8 Threshold-voltage shift of a-IGZO FETs along with stress time under positive gate bias temperature stress ($V_{GS} = 20$ V and $V_{DS} = 0$ V for 5000 s at 30 °C)

2.4 Conclusion

I demonstrated an air stable n-type C₆₀ OFET by using a perfluorinated polymer, CYTOP, as the gate dielectric layer. Replacing the gate dielectric material by SiO₂ resulted in no transistor action in ambient air. The device showed similar device characteristics as the encapsulated device fabricated on SiO₂ gate dielectric layer. This indicates that the interface trap density for electrons for n-type organic materials is significantly reduced by using the perfluorinated polymer as the gate dielectric layer even in ambient air.

Moreover, the FETs with CYTOP passivation layer successfully exhibited a relatively good electrical characteristic and stability compared with that of the device with a SiO_x-passivation layer or the non-passivated device.

I believe that these findings are important for the realization of organic based complementary metal–insulator–semiconductor (CMOS) circuits.

2.5 Bibliography

1. A.R. Murphy, M.J. Frechet, Chemical Reviews, **107**, 1066 (2007)
2. C.R. Newman, C.D. Friebie, D.A. da Silva Filho, J. Bredas, P.C. Ewbank, K.R. Mann, Chemistry of Materials, **46** , 4436 (2004)
3. S. Ando, J. Nishida, H. Tada, Y. Inoue, S. Tokito, Y. Yamashita, Journal of the American Chemical Society, **127**, 5336 (2005)
4. R.J. Chesterfield, J.C. McKeen, C.R. Newman, C.D. Frisbie, Journal of Applied Physics, **95**, 6396 (2004).
5. S. Kobayashi, T. Takenobu, S. Mori, A. Fujiwara, Y. Iwasa, Applied Physics Letters, **82**, 4581 (2003)
6. L.-L. Chua, J. Zaumseil, J.-F. Chang, E. C.-W. Ou, P. K.-H. Ho, H. Sirringhaus, R.H. Friend, Nature, **434**, 94 (2005)
7. Z. Bao, A.J. Lovinger, J. Brown, Journal of the American Chemical Society, **120** , 207 (1998)
8. Y. Hosoi, D. Tsunami, H. Ishii, Y. Furukawa, Chemical Physics Letters, **436**, 139 (2007).
9. H.Z. Chen, M.M. Ling, X. Mo, M.M. Shi, M. Wang, Z. Bao, Chemistry of Materials, **19**, 816 (2007)
10. Q. Tang, H. Li, Y. Liu, W. Hu, Journal of the American Chemical Society, **128**, 14635 (2006)

11. M.M. Ling, P. Erk, M. Gomez, M. Koenemann, J. Locklin, Z. Bao, *Advanced Materials*, **19**, 1123 (2007)
12. H.E. Katz, J. Johnson, A.J. Lovinger, W. Li, *Journal of the American Chemical Society*, **122**, 7787 (2000)
13. R.C. Haddon, A.S. Perel, R.C. Morris, T.T.M. Palstra, A.F. Hebard, R.M. Fleming, *Applied Physics Letters*, **67**, 121 (1995)
14. A. Tapponnier, I. Biaggio, P. Gu ¨ nter, *Applied Physics Letters*, **86**, 12114 (2005)
15. W.L. Kalb, T. Mathis, S. Haas, A.F. Stassen, B. Batlogg, *Applied Physics Letters* **90** 092104 (2007)

3 . In Situ Antibody Detection Using Aqueous Stable Pentacene Transistor Biosensors

3.1 Introduction

As the demand for diagnostic laboratories continues to increase with increased health care costs, the necessity for rapid and inexpensive medical analyses has become increasingly apparent. The use of optical measurements is predominant, but this method has several limitations due to the required fluorescent dyes and expensive detectors.¹ In addition, because optical equipment is not portable, in vivo and in situ measurements are also very difficult. Recent advances in bio-chemical detection research, in part benefiting from the overwhelming progress made in organic electronics, have shown great promise for a viable, low-cost alternative to current optical detection systems.²

Micro-biosensors based on OFETs have recently attracted a considerable amount of attention owing to their potential for miniaturization, standardization, mass-production and a suitable configuration for smart sensor.^{3,4} Recent advances in chemical

detection research, in part benefitting from the overwhelming progress made in nanotechnology and organic electronics, have shown great promise for a viable, low-cost alternative to current optical detection systems.² Many examples exist for the detection of analyte vapors using an OFET platform, with numerous reports addressing the ability to identify particular analytes either through the use of a fingerprint response^{5,6} or by incorporating selective detection layers on functional OFETs;⁴ however, these devices were not selective toward a particular analyte. Selective in situ detection with OFETs requires a versatile method for the immobilization of various selective molecular probes, which is not a trivial task. Additionally, it is well-known that most microorganisms possess a negative surface charge under physiological conditions.⁷ Therefore, developing complementary tools for probing analyte surface charges on a nanoscale level is a highly relevant challenge in cellular microbiology and biophysics.

However, the development of devices based on an air/aqueous stable organic semiconductor still faces many challenges. The open morphology with large clefts between the grains of polycrystalline organic molecules limits the charge transport, which shortens the life of the devices due to degradation of the materials.⁸⁻¹⁰ Another relevant

issue is the method of encapsulation or surface modification, which are both considered to be unfavorable due to solution processing issues.^{3,11}

In this research, pentacene transistor was used to bio-chemical sensors in aqueous media with a spin-coated CYTOP passivation. First, working stability in aqueous media is characterized. After that, maleic anhydride (MA) layers was deposited for chemically functionalize the OFET surface. Bovine serum albumin (BSA) was covalently attached to the ppMA functional layer as a catcher probe and proven to be effective for the detection of antibodies.¹² Anti-BSA was selectively detected using OFET, and the results were corroborated with a well-characterized optical detection method, SPR.

3.2 Experimental

All materials were purchased from Aldrich and were used as received without further purification unless otherwise stated. N-ethyl-N-(3-dimethylaminopropyl)-carbodiimide hydrochloride (EDC) and N-hydroxysuccinimide (NHS) were purchased from Fluka and rabbit monoclonal antiBSA was obtained from Millipore.

The fabrication of the bottom-contact pentacene transistor is schematically illustrated in Figure 3.1. A heavily doped silicon wafer was used to fabricate the bottom-contact OFETs. The substrates were cleaned using acetone, 2-propanol, ethanol; rinsed with deionized water; and then baked at 100 °C for 5 min. CYTOP solution (1 wt %) was spincoated at 4000 rpm for 40 s in an Ar-filled glovebox and baked at 80 °C for 30 min and 180 °C for 1 h to achieve a required thickness of 15 nm. CYTOP insulating films have already proven to be highly stable in air and moisture¹³ with a surface roughness of 0.6 nm, as determined by AFM. 50 nm- thick source-drain electrodes with a width (W) of 500 μm and length (L) of 50 μm were deposited and patterned using a shadow mask. The Au electrodes were treated for 1 h with 0.1mM solution of 2-mercapto-5-nitrobenzimidazole (MNB) diluted in ethanol to reduce the contact resistance.¹⁴ Finally, a 30 nm

thick pentacene film was thermally deposited under a pressure of 6.5×10^{-7} torr with a deposition rate of 0.5 \AA/s at a surface temperature of 30°C and displays a surface peak-to-valley roughness of 30 nm. The optical device fabrication, identical to that of the OFETs, was done using similar procedures as previously reported.³

The CYTOP layer was deposited by spin-coating for passivation and polymerization of MA was carried out in a home-built PECVD reactor.³ All electrical measurements were performed with a Agilent 4155C semiconductor characterization system in ambient air and aqueous media. The optical detection was done with a home-built surface plasmon resonance (SPR) spectroscopy.¹⁵

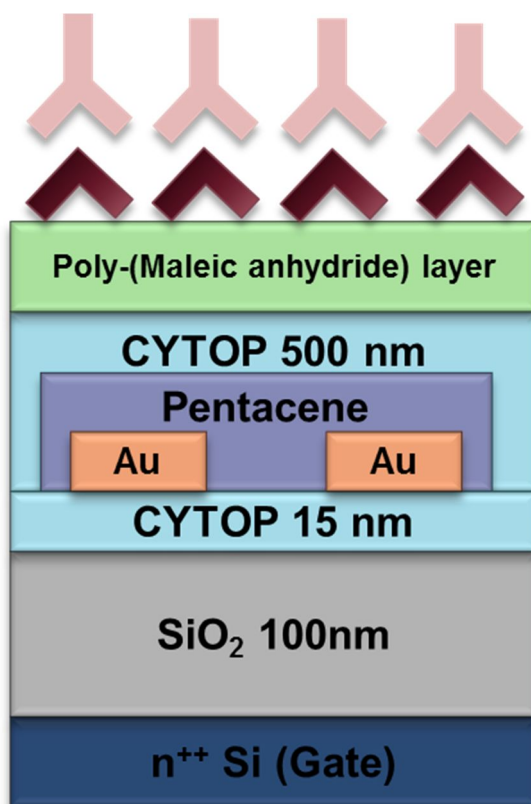


Figure 3.1 Schematic structure of bio-sensitive OFET for anti-BSA detecting

3.3 Result and Discussion

3.3.1 FET characteristics in aqueous media

Pentacene has become the most widely studied organic semiconductor due to its excellent transport properties; however, it suffers from poor stability in ambient conditions.¹⁶ Air-stable bottom contact OFETs with a 30 nm thick pentacene layer on an ultrathin CYTOP (15 nm) layer were fabricated and then spincoated on the Si substrate covered with 200 nm thick SiO₂. The device exhibited excellent linear and saturation regime characteristics with a V_{DS} of -50 V, an average mobility of 0.064 cm²/V s, an on/off ratio of 10⁴, and a threshold voltage (V_{th}) of -3.4 V. The transfer and output characteristics of these devices are displayed in Figure 3.2.

Prior to sensor analysis, the functional OFET surface was characterized in ambient and aqueous conditions. The source-drain current (I_{DS}) in buffer solution (Red and yellow curve) was not changed compared to ambient air (black and grey curve, Figure 3.2) at a low drain voltage of -5 V, which is necessary for operation in the buffer solution. The slight variation in the transfer characteristics illustrates a relatively stable behavior with a small change in mobility

from $0.064 \text{ cm}^2/\text{V s}$ in ambient air to $0.058 \text{ cm}^2/\text{V s}$ in the buffer solution. The other characteristics are described in table 3.1. This indicates that the passivation by the thin perfluorinated polymer layer is very effective to protect the pentacene layer from water permeation.

After that, the working stability of OFET in aqueous media was investigated. Figure 3.3 is the changing of transfer characteristics as time passage with buffer solution. Before optimization of passivation layer deposition, the transfer curve changed rapidly in water. It is almost impossible to detect bio-molecule because degradation of current is much larger than sensing signal. So passivation layer thickness and annealing temperature was changed to 500 nm and 130°C . After optimization, transfer characteristics are changed to stable. And changing of mobility and threshold voltage shift are summarized in Figure 3.4.

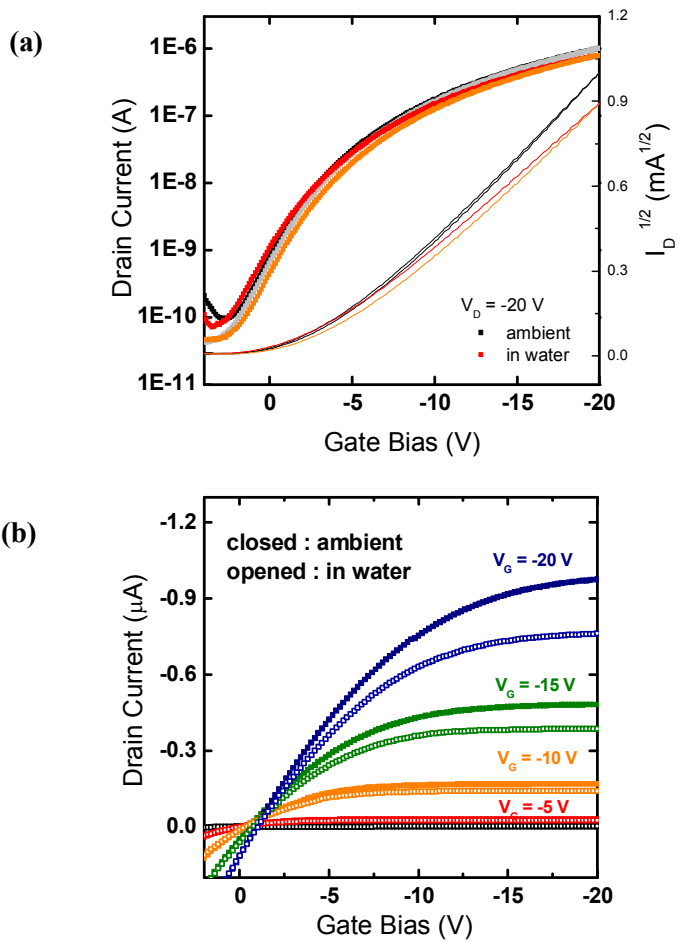


Figure 3.2 (a) Transfer characteristics and (b) Output characteristics of OFET working in water

	Ambient air	In water
Mobility	0.064	0.058
V_{TH}	-3.4	-3.3
On/Off	2.1×10^4	1.8×10^4

Table 3.1 Electrical parameter difference in working environment

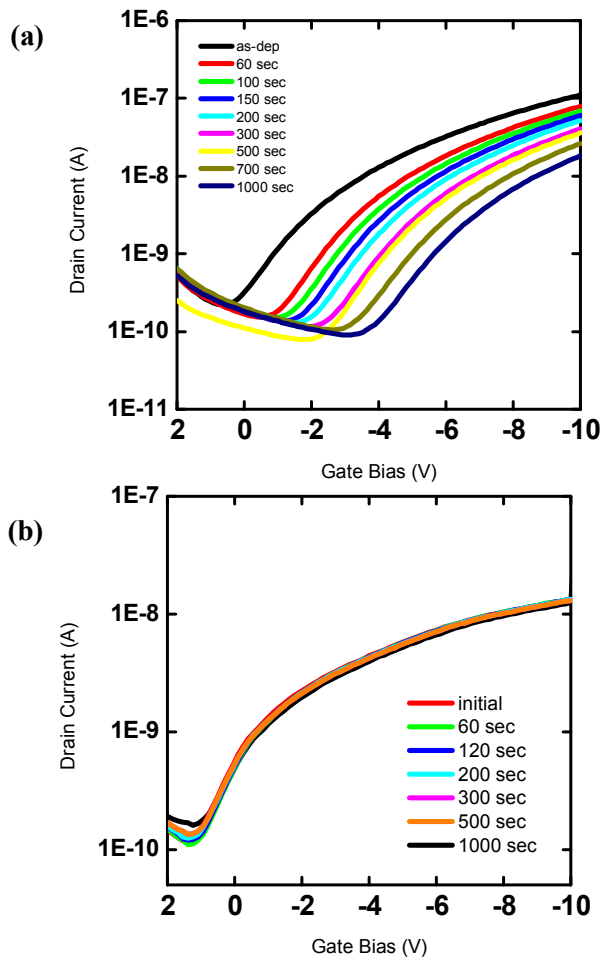


Figure 3.3 Changing of transfer characteristics as time passage with (a) non-optimized device (b) optimized device

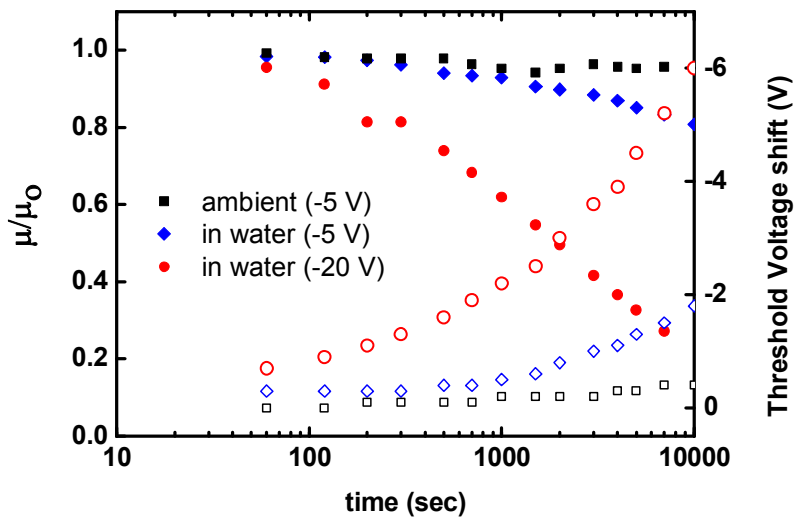


Figure 3.4 Change of Mobility and threshold voltage shift as working condition

3.3.2 Chemical responsivity

Biosensing experiments, particularly antibody–antigen interactions, depend mainly on the pH of the working solution due to the different isoelectric point (pI) of proteins. Thus, the sensitivity and long-term stability of all three devices were initially examined in parallel by exposing the unfunctionalized OFET channel to different pH solutions. In PBS, the baseline I_{DS} was recorded after 60 s of constant bias (a drain-source bias $V_{DS} = -2$ V and a gate bias $V_G = -5$ V) prior to the injection of the pH solution. Next, three solutions with pH 11, 7 and 4 at a concentration of 10 mM were injected sequentially onto the device. The recorded value of I_{DS} against time is shown in Figure 3.5 (a) and saturated transfer characteristic is shown in Figure 3.5(b). Between each trial, the device was rinsed extensively with PBS to restore the baseline I_{DS} . I observed an increase in I_{DS} with the acidity (pH 4) and a decrease with the basicity (pH 11) of the solution.

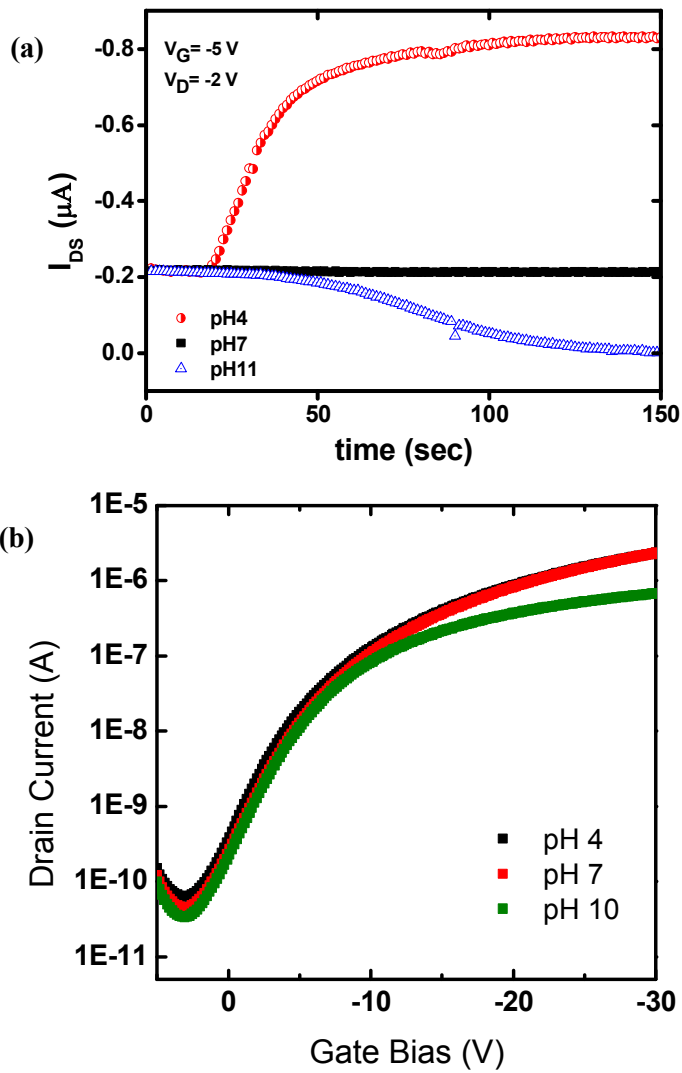


Figure 3.5 (a) The current response with various pH value (b) The transfer characteristic with various pH value

3.3.3 Antibody detection

Electrical and sensing measurements in the buffer solutions were done using a flow cell, which was laminated on the PE-CVD-treated OFET surface. PE-CVD provides a single step process at room temperature, resulting in a conformal coating with excellent adhesion to the underlying film. In the presence of a buffer solution (pH 7, 10 mM), the anhydride groups on the ppMA surface were hydrolyzed and converted to carboxylic acids and then activated by circulating a solution containing 0.2 M EDC and 0.05 M NHS at a constant rate of 300 $\mu\text{L}/\text{min}$ for 20 min. BSA was covalently attached to the surface from a 1 μM BSA solution for 80 min, after which any nonchemically bound material was rinsed with buffer solution. The transfer characteristics in air at a V_{DS} of -5 V showed a shift in V_{th} after the PE-CVD treatment, which can be attributed to charge trapping at the interface during the deposition process. Moreover, the OFET drain current decreased after BSA attachment due to the negative charges on the BSA proteins under the given operating conditions. Control experiments were carried out to confirm the covalent attachment of BSA with the sensors surface using in situ SPR measurements. The

specificity of these sensors toward the antibody was evaluated using antiBSA.

Antigen/antibody interactions belong to a large group of noncovalent biological binding reactions, which depend mainly on complementary structures between a ligand and a binding site (receptor) on a macromolecule. Since the antigen and antibody consist of amino acids bearing charges, we expect that the polarity of these charges strongly depends on the pH and ionic strength of the aqueous phase, which determines the charged states and binding kinetics. This polarity is normally defined by the isoelectric point (pI) of a respective analyte. The pI of the bovine serum is at pH 5.4, which means that the amino acids within the BSA proteins will contain (on average) negative charges above this pH. We expect that negatively charged BSA proteins will result in a decrease in the current during sensor operation and vice versa.

The sensor performance of the OFETs was evaluated under constant bias conditions. The change in current was recorded while switching from a baseline buffer solution to one containing a given concentration of antiBSA. Typically, the baseline current was recorded for 100 s with a constant source-drain and gate biases ($V_{DS} = -2$ V, V_G

= -5 V) prior to analyte injection. A flow rate of 300 $\mu\text{L}/\text{min}$ was used to minimize the mass transfer limitations of the analyte to the sensor surface, which has been shown to occur below 20-30 $\mu\text{L}/\text{min}$.¹⁷ A 500 nM solution of antiBSA at pH 7 was injected into the flow cell while recording the I_{DS} under constant bias conditions as described above. Equilibrium between the bulk concentration and the corresponding surface coverage was achieved within 250 s, as determined by the source-drain current with the time profile (i.e., I_{DS} is constant after surface equilibrium is achieved). The solution was then switched to the buffer solution (pH 7), and the I_{DS} recovered to the initial baseline current after 130 s (black curve in Figure 3.6 (a)). Next, a new baseline was established in a 10 mM buffer solution at pH 5. In a similar manner to the pH 7 case, a 500 nM concentrated antiBSA solution diluted in buffer at pH 5 was introduced to the sensor surface while recording the I_{DS} (blue curve in Figure 3.6(a)). However, at this pH, the I_{DS} increased as the antiBSA reached the sensor surface, and the sequential exchange of antiBSA with buffer solution (pH 5) resulted in a decrease in the I_{DS} . Two effects on the I_{DS} were observed in response to antiBSA: (a) the magnitude of the change in current (ΔI_{DS}) at pH 7 was a factor of 5 time less than at pH 5, and (b) the

polarity of the current change was opposite at pH 7 from pH 5. These experimental results are consistent with our initial hypotheses that an opposite change in current would occur above and below the pI. For comparison purposes, optical measurements were taken using a home-built SPR spectroscopy¹⁵ to corroborate the OFET response on an identical substrate. SPR spectroscopy also measures the label-free binding by directly monitoring the change in the refractive index at the biosensor surface, and the response is proportional to the mass of the bound analytes.¹⁸ In a typical optical measurement, a kinetic scan of the minimum resonance angle shift (RAS) with time is performed. The black curve in the Figure 3.6(b) shows the change in RAS after injection of 500 nM antiBSA and during the formation of the immunoassay, which occurred over a period of 150 min. Careful rinsing with buffer solution (pH 7) was then performed, showing a small effect on the adsorbed antiBSA layer thickness. A similar experiment was done using antiBSA diluted in pH 5 buffer solution with the same concentration (blue curve). Clearly, the SPR measurements could not discriminate between the polarities of the charged states in the antiBSA. Apart from charge discrimination, the surface titration experiments were also performed to quantify the

amount of antiBSA selectively adsorbed on the sensor surface. The change in I_{DS} with time contains kinetic information on the immunoassay and can be analyzed to determine association (k_{on}) and dissociation (k_{off}) rate constants. The general procedure begins with injecting an analyte solution at low concentration and allowing the adsorption of antiBSA onto BSA to reach equilibrium. This process is repeated with higher concentrations until the surface is saturated with the target analyte. In the first experiment, a baseline current was established in 10 mM buffer solution (pH 7) followed by a solution exchange with a 10 nM solution of antiBSA at pH 7. I_{DS} were measured until equilibrium was achieved, as indicated by the constant source-drain current. Next, solutions with concentrations of 50, 100, 200, 500, and 1000 nM antiBSA were injected into the flow system (see thin arrows in Figure 3.7(a)), which resulted in correspondingly higher equilibrium surface coverage. Finally, the antiBSA solution was exchanged by the buffer solution (pH 7) in order to dissociate the bound species. Similar surface titration measurements were repeated with antiBSA in buffer solutions at pH 5. As shown in Figure 3b, surface coverage equilibrium was achieved at a rather high concentration of antiBSA at pH 5. In each case (Figure 3.7 (a) and (b)),

a rapid decrease in the I_{DS} was observed within the initial 40 s after the antiBSA solution was replaced by the buffer solutions, owing to the removal of physisorbed antiBSA, which accounted for 35% and 51% of the equilibrated IDS at pH 7 and pH 5, respectively. In order to validate the performance of the electronic device, kinetic titration measurements were taken using SPR, where the RAS was measured for various antiBSA concentrations at pH 7 and pH 5 (Figure 3.6 (c) and (d)). The calculated thicknesses of BSA and antiBSA layers on the OFET surface were 4 and 3.8 nm, respectively.^{19,20} AntiBSA/BSA binding occurred at a much slower rate during the SPR measurements, leading to a time constant of tens of minutes. OFET sensor measurements showed a 1 order of magnitude faster response time compared to the SPR method, which can be attributed to the enhanced diffusion/adsorption induced by the electric field present during OFET operation. During the SPR measurements, only a very small change in RAS was observed upon dissociation of antiBSA (Figures 3.5(b) and 3.6 (c), (d)). It is likely that multisite complexes are formed, leading to stronger protein-protein binding through the multiple available sites, mass transport, crowding, or denaturing of protein.²¹ These factors introduce additional complexity to the analysis of the protein rate

constant that is not directly related to the association or dissociation reactions. Additionally, the events occur on a time scale that cannot accurately be resolved by SPR measurements.^{21,22} The accuracy of quantifying the kinetic parameters is limited by the stronger binding observed in the SPR measurements. The K_A ($K_A = k_{on}/k_{off}$, based on the Langmuir model²³) values obtained using the OFET sensor were an order of magnitude higher than the SPR sensors and 4 times higher than previously reported values.²⁴ However, Ishikawa et al. showed values 1 order of magnitude higher for the K_A for N-protein using In₂O₃ nanowire transistor based sensors.²⁵ Regardless, many advantages exist for using organic devices with low-cost and simple processing methods.

The effect of pH on the affinity constant is also significant for OFET sensors. The discrimination factor in K_A found at pH 7 was an order of magnitude higher than at pH 5. Detection with SPR, however, showed a relatively minor difference (less than a factor of 2) between pH 7 and pH 5. During sensor measurements with the OFETs, the solution pH influences the polarity and magnitude of the drain current response, which is related to protein binding. To explain the differences in the surface charge density of a protein, I propose

models for BSA/antiBSA binding in pH 5 (Figure 3.7(a)) and in pH 7 (Figure 3.7(b)) buffer solutions. It has been previously reported that in the case of bovine serum, a change in the electric flux is very small when varying pH below the pI.²⁶ Therefore, I assumed that due to the flux effect, the ratio of NH₂ to NH₃ is high below the pI, resulting in a weak Coulombic repulsion between BSA and antiBSA. Thus, more antiBSA can adsorb, leading to surface saturation occurring at higher concentrations. This assumption agrees well with the observed experimental data for titration (Figure 3.6(b)). The presence of such weak repulsive interactions that are proportional to the square of the surface charges³⁴ leads to creation of a strong repulsive barrier between transistor channel and the surface-bound analytes (Figure 3.7(a)). Ultimately, the holes in the channel region accumulate more efficiently, and an increase in IDS with a larger magnitude of current change (more species adsorbed to influence the current) [Figures 3.5(a) (blue curve) and 3.6(b)] is seen. A larger change in electric flux occurs at pH values above the pI, which results in a high density of COO⁻ in the BSA/antiBSA complex and a strong Coulombic repulsion between BSA and antiBSA. This strong electrostatic repulsion allows for a lower density of negative charges at the sensor surface. These low

densities of negative charges subsequently show a weak electrostatic interaction between the channel region and the surface negative charges, as shown in Figure 4b. Essentially, the holes are depleted from the channel region of the transistor, increasing the overall channel resistance.

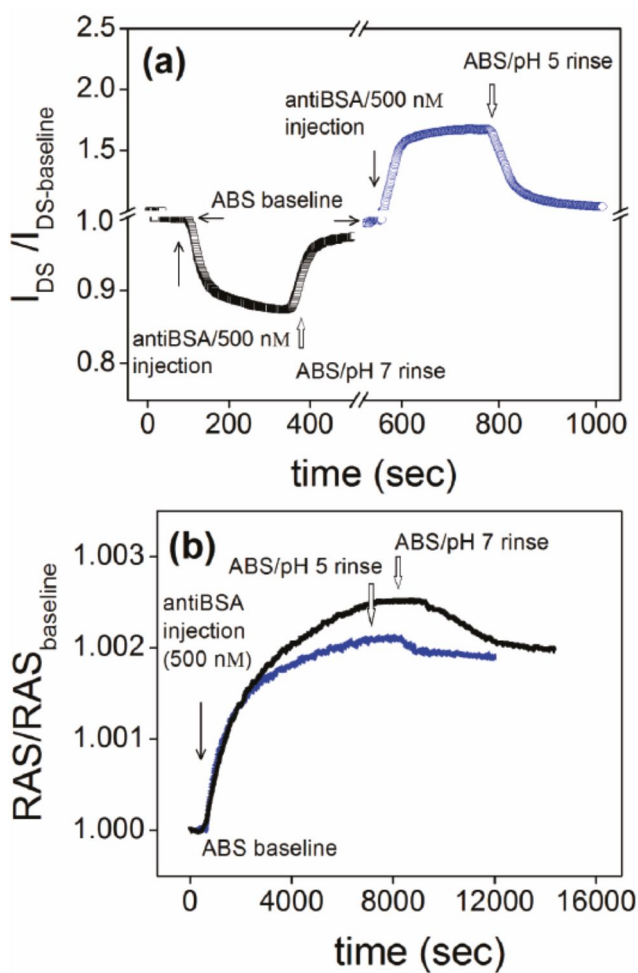


Figure 3.6 Charge discrimination experiments for BSA/antiBSA immunoassay formation in aqueous buffer solutions at different pHs using (a) OFET and (b) SPR sensors

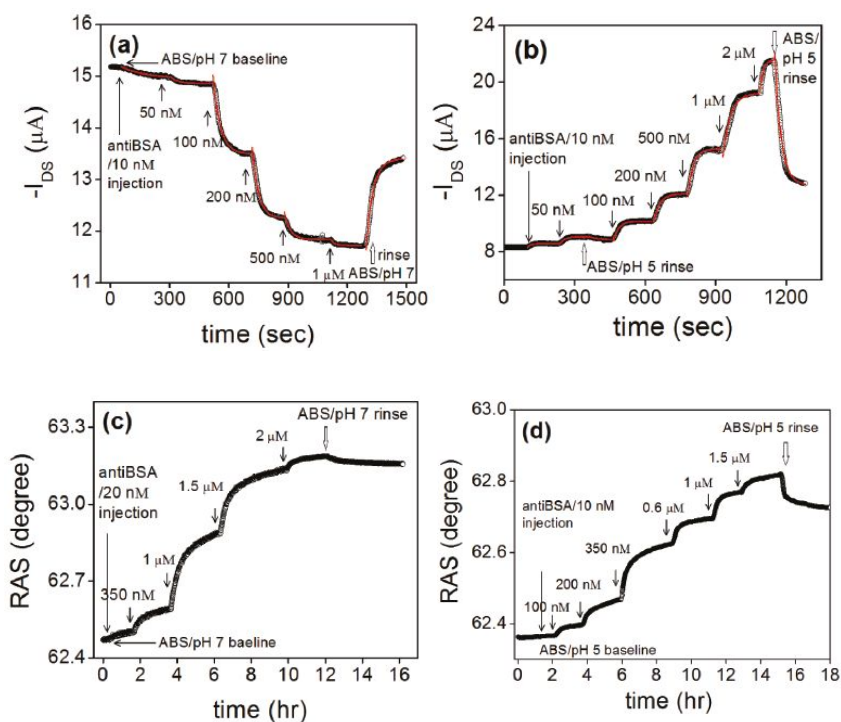


Figure 3.7 Titration curves for BSA/antiBSA immunoassay formation using OFET and optical sensors. Solid arrows indicate the additions of antiBSA solutions and open arrows indicate the exchange with buffer solution. Red solid curves represent the Langmuir fits. OFET current response with exposure to antiBSA solutions at (a) pH 7 and (b) pH 5. SPR sensor titration with antiBSA solutions at (c) pH 7 and (d) pH 5.

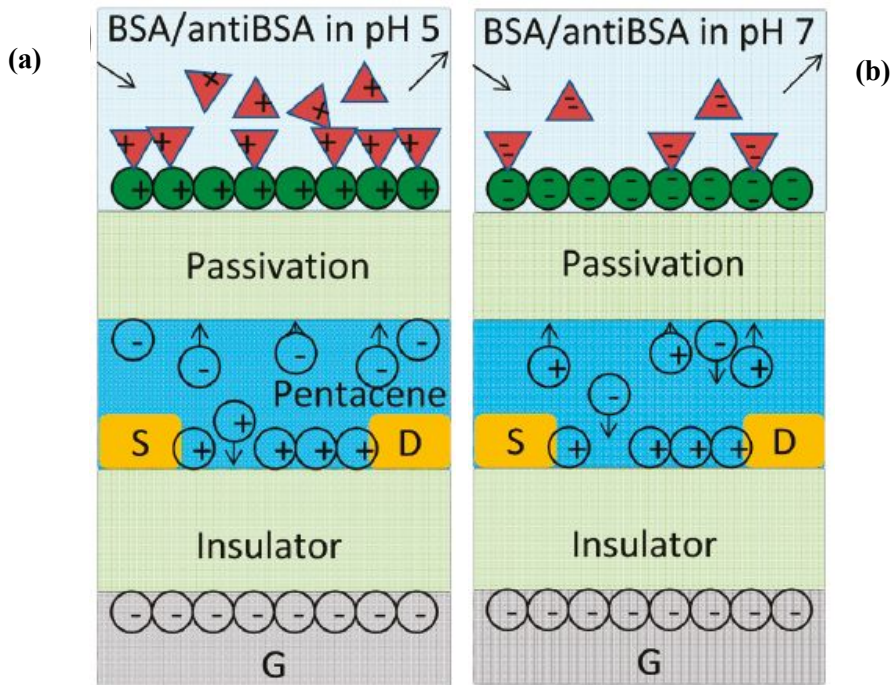


Figure 3.8 The model for immunodetection using pentacene transistor sensors when antiBSA is diluted in buffer solution at (a) pH 5 and (b) pH 7.

3.4 Conclusion

I have demonstrated a highly sensitive, low cost, fast, and selective immune-transistor sensor with analyte charge discrimination at variable pH's. A Langmuir model was used to fit the titration curves, which showed that a high affinity constant [$K_A = (1.1 \pm 3) \times 10^7 \text{ M}^{-1}$] can be achieved in an organic transistor based detection system when antiBSA was diluted at pH 7. Remarkably, the affinity constant determined at pH 7 was 1 order of the magnitude higher than those obtained on identical substrates using a well-defined optical technique, surface plasmon resonance (SPR) spectroscopy, with the additional advantage of charge discrimination. Due to the fast binding process on the OFETs sensor surface, one could easily prevent the undesirable reactions that occur during SPR measurements. My approach appears to have potential for extension into a fully integrated system, providing an inexpensive, fast, and selective sensor platform for a wide range of applications in biomedical use, gene therapy, and microarrays as well as screening for the affinity constant of specific antibodies generated by a library of cells.

3.5 Bibliography

1. Neumann, T., Johansson, M.L., Kambhampati, D., Knoll, W., Adv. Funct. Mater. **12**, 575–586 (2002)
2. Roberts, M.E., Mannsfeld, S.C.B., Queralto, N., Locklin, J., Knoll, W., Bao, Z., Proc. Natl. Acad. Sci. U.S.A. **105**, 12134 (2008).
3. Khan, H.U., Roberts, M.E., Johnson, O., Foerch, R., Knoll, W., Bao, Z., 2010. Adv. Mater. 22 (40), 4452–4456.
4. Torsi, L., Farinola, G.M., Marinelli, F., Tanese, M.C., Omar, O.H., Valli, L., Babudri, F., Palmisano, F., Zambonin, P.G., Naso, F., 2008. Nat. Mater. 7 (5), 412–417
5. Crone, B.; Dodabalapur, A.; Gelperin, A.; Torsi, L.; Katz, H. E.; Lovinger, A. J.; Bao, Z. Appl. Phys. Lett., **78**, 2229 (2001)
6. Chang, J. B.; Liu, V.; Subramanian, V.; Sivula, K.; Luscombe, C.; Murphy, A.; Liu, J.; Frechet, J. M. J. J. Appl. Phys., **100**, 014506. (2006)
7. Mozes, N.; Marchal, F.; Hermesse, M. P.; Van Haecht, J. L.; Reuliaux, L.; Leonard, A. J.; Rouxhet, P. G. Biotechnol. Bioeng. **30**, 439. (1987)
8. Dimitrakopoulos, C.D., Mascaro, D.J., 2001. IBM J. Res. Dev. 45 (1), 11–27.

9. Zhu, Z.T., Mason, J.T., Dieckmann, R., Malliaras, G.G., 2002. Appl. Phys. Lett. 81 (24),4643–4645.
10. Andraz, P., Gvido, B., 2009. Appl. Phys. Lett. 94 (12), 123301–123303.
11. Sreenivasan, R., Gleason, K.K., 2009. Chem. Vap. Deposition 15 (4–6), 77–90.
12. Chiem, N. H.; Harrison, D. J. Electrophoresis, **19**, 3040 (1998)
13. Walser, M. P.; Kalb, W. L.; Mathis, T.; Brenner, T. J.; Batlogg, B. Appl. Phys. Lett., **94**, 053303 (2009)
14. Park, D. S.; Jang, W. C.; Cho, S. W.; Seo, J. H.; Jeong, I. S.; Kim, T. W.; Chang, G. S.; Moewes, A.; Chae, K. H.; Jeong, K.; Yoo, K.-H.; Whang, C. N. Org. Electron., **9**, 1010. (2008)
15. Knoll, W. Annu. Rev. Phys. Chem., **49**, 569 (1998)
16. Klauk, H.; Halik, M.; Zschieschang, U.; Schmid, G.; Radlik, W.; Weber, W. J. Appl. Phys., **92**, 5259 (2002)
17. Adamczyk, M.; Moore, J. A.; Yu, Z. Methods, **20**, 319 (2000)
18. Stenberg, E.; Persson, B; Roos, H.; Urbaniczky, C. J. Colloid Interface Sci., **143**, 513 (1991)
19. Terashima, H.; Tsuji, T. Colloids Surf. B. Biointerfaces, **27**, 115 (2002)

20. Tronin, A.; Dubrovsky, T.; Nicolini, C. *Thin Solid Films*, **894**, 284 (1996)
21. Schreiber, G.; Haran, G.; Zhou, H.-X. *Chem. Rev.*, **109**, 839 (2009)
22. Rich, R. L.; Cannon, M. J.; Jenkins, J.; Pandian, P.; Sundaram, S.; Magyar, R.; Brockman, J.; Lambert, J.; Myszka, D. G. *Anal. Biochem.*, **373**, 112 (2008)
23. Langmuir, I. *J. Am. Chem. Soc.*, **40**, 1361 (1918)
24. Li, B.; Chen, J.; Long, M. *Anal. Biochem.*, **377**, 195 (2008)
25. Ishikawa, F. N.; Chang, H.-K.; Curreli, M.; Liao, H.-I.; Olson, A. C.; Chen, P.-C.; Zhang, R.; Roberts, R. W.; Sun, R.; Cote, R. J.; Thompson, M. E.; Zhou, C. *ACS Nano*, **3**, 1219 (2009)
26. Chun, K. Y.; Stroeve, P. *Langmuir*, **18**, 4653 (2002)
27. Burns, D. B.; Zydney, A. L. *Biotechnol. Bioeng.*, **64**, 27 (2000)

4 . Effect of n-type doping to Organic Field

Effect Transistors

4.1 Introduction

Organic Field Effect Transistors (OFETs) have attracted recently because of their high potential for flexible, large-area, low-cost, and ultrathin electronics. Soluble polymeric semiconducting material is strong candidate to realize these advantages. Various polymeric materials are reported with high FET mobility more than $1.0 \text{ cm}^2/\text{V}\cdot\text{sec}$,¹⁻⁶ comparable to amorphous silicon FET. That is enough value for driving circuit in display panel but polymeric complementary integrated circuit is still hard to realize due to unbalancing of n-type components. Generally, n-channel polymers have lower mobility and stability than p-channel polymers due to difficulty of material synthesis with deep-lying Lowest Unoccupied Molecular Orbital(LUMO) under the trap sites generated by hydrogenated oxygen,⁷ located near 3.6~4.0 eV. The n-channel transporting polymer satisfied that of LUMO level such as dithiophene-alkylimide⁸ and perylene^{9, 10} derivatives are

representative results for performance and ambient-air stability.

The polymers with electron accepting naphthalene-bis(dicarboximide)(NDI) core are promising material for challenge to high performance and operational stability in n-channel operation. Poly{[N,N9-bis(2-octyldodecyl)-naphthalene-1,4,5,8-bis(dicarboximide)-2,6-diyl]-alt-5,59-(2,29-bithiophene)} (P(NDI2DO-T2), Polyera Activink N2200)¹¹⁻¹³ and poly[(E)-2,7-bis(2-decyltetradecyl)-4-methyl-9-(5-(2-(5-methylthiophen-2-yl)vinyl)thiophen-2-yl)benzo[*lmn*][3,8]phenanthroline-1,3,6,8(2H,7H)-tetraone](PNDI-TVT)¹⁴ were reported to achieve electron mobility of 0.85 cm²/V•sec and 1.8 cm²/V•sec, respectively. Strong π - π interaction provided by planar conjugated bicyclic structure could contribute to enhancement of greater electron mobility. Moreover, high air-stability is achieved as result of pulling down the LUMO level due to electron withdrawing diimide group for each naphthalene moiety.¹⁴ Despite of improved mobility and stability of NDI-based n-transporting polymer, there are still remained a situation capable of performance enhancement by applying of doping technique. Doping to semiconducting layer is one of method to enhance conductivity and to reduce contact resistance for organic opto-

electronic devices such as light emitting diodes (OLEDs) or photovoltaics (OPVs) because of increased carrier density transferred from doped materials.¹⁵⁻¹⁷ The deactivation of trap sites by low concentration of n-type dopant is recently reported.^{7, 18, 19} But the application of doping to organic field effect transistor needs quite different approach in two point of view. The first one is microstructure of material. General OLED devices require amorphous semiconductor to prohibit quenching or recombination of carrier but organic semiconductors for FET device are preferred to use highly crystalline structure to maximize carrier mobility. Therefore it should be considered to determine the effect of dopant molecules to crystallinity of host semiconductor.²⁰⁻²³ The molecular patch doping to increase mobility and reduce threshold voltage is one of good example doping technic without influencing to crystallinity of pentacene.²⁴ The second one is increased conductivity by doping could influence to on/off ratio of OFET device by also increased off-current. To avoid this problem, low-concentration doping to semiconducting layer or selective doping method on/under the contact region are suggested.^{23, 25, 26}

I investigated the electrical property of n-type doped polymeric OFET with low-concentration doping and less crystalline material.

The P(NDI2DO-T2), representative NDI-based material is selected for semiconducting layer due to its high electron transporting characteristics and stable property in ambient air. The unconventional microstructure of this polymer reported to have weak crystallinity to out-of-plane direction and predominantly face-on molecular packing to in-plane direction.²⁷ This microstructure can be expected to minimize the distortion by adding the dopants. In contrast to p-type doping, the molecular n-type doping is more difficult due to energetic position of the orbitals required above the LUMO of P(NDI2DO-T2) located at -4.0 eV,¹³ which makes such dopant materials unstable against oxygen. Two kind of dopant were investigated which are the strongly reducing molecule, bis(cyclopentadienyl)-cobalt(II) (cobaltocene, C_{ocp}₂) having an ionization energy of 4.0 eV²⁸ and the alkali metal salts, CsF. To increase operational stability of n-type OFET the CYTOP gate-dielectric insulator was considered to avoid the generation trap site.²⁹ The chemical structures of these materials are shown in Figure 4.1. As the result of doping, here, I report that P(NDI2DO-T2) material exhibited a 2 times increased n-type mobility, reduced threshold voltage and increased reliability in bias stress cycles. The Grazing Incidence X-

Ray Diffraction (GIXRD) analysis was followed for finding out the reason. I can expect to get higher performance to other n-type polymer FET with these results and it can be applied to realize the printed CMOS circuits.

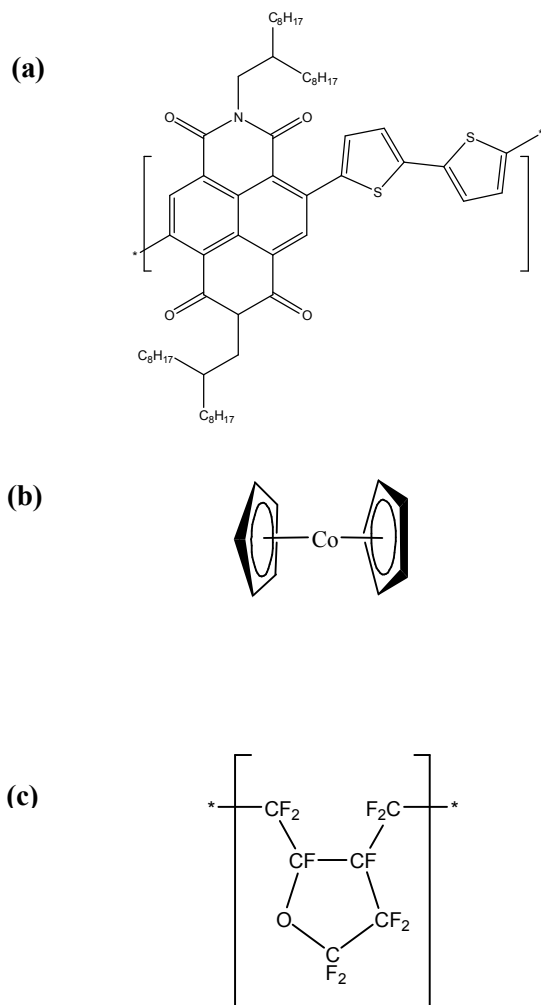


Figure 4.1 Chemical structure of (a) P(NDI2OD-T2) (b)

Cocup₂ and (c) CYTOP

4.2 Experiment

To investigate the electrical characteristics of n-type doped OFET, I considered devices with top-gate and bottom-contact architecture. This structure was used because of low contact resistance to carrier injection and better processability with photolithography.³⁰ Figure 4.2 shows the schematic structure of TG/BC OFET device. The Source and drain electrodes are Cr/Au(3 nm/27 nm) patterned on glass substrate. Channel length and width are 10 μm and 1000 μm , respectively. Small quantity of C₆₀ and CsF dopants are dissolved in 2-ethoxyethanol and mixed P(NDI2DO-T2) dissolved in p-xylene with following weight ratios : 0.0%, 0.025%, 0.5%, 1.0% and 2.0%. Higher mixing ratio makes aggregation of dopants on film. Doped P(NDI2DO-T2) deposited by spin-casting and dried at 110°C. The thickness of spin-casted film was 30 nm measured by PSIA XE-100 Atomic Force Microscopy. CYTOP dielectric insulator selected because its hydroxyl-free interface can reduce trap-sites and increase device stability. It is also important reason that perfluorotrialkylamine, solvent of CYTOP, is orthogonal solvent to P(NDI2DO-T2) or dopant molecules. CYTOP deposited by spin-casting with 50 nm thickness and annealed at 130°C for 1 Hr. Every spin-casting process was done

in N₂ filled glove box. The Al (50 nm) gate electrode was deposited by thermal evaporation in high vacuum condition and patterned with shadow mask. The electrical characteristics of devices were measured with Agilent 4156A Semiconductor Parameter Analyzer in N₂ filled glove box. The dielectric permittivity of CYTOP insulator was 2.1 and FET mobility is calculated in the saturation regime using **Equation 1**. The subthreshold swing (S.S.) was calculated using **Equation 2**. The cyclic bias stress was applied to investigate operational stability with 1000 times of gate bias sweep in N₂ filled glove box. This measurement was done within 8 Hr, enough time to disregard the degradation of semiconductor molecule.

$$I_{D,sat} = \frac{W}{2L} C_{ox} \mu (V_G - V_T)^2 \quad (1)$$

$$S.S. = \left[\frac{d \log(I_D)}{d V_G} \right]^{-1} \quad (2)$$

In order to investigate the structure of the P(NDI2DO-T2) Grazing Incidence X-Ray Diffraction (GIXRD) measurement were carried out at the 5C beam line at the Pohang Accelerator Laboratory (PAL), Korea. The samples for x-ray measurement are fabricated on soda-lime bare glass. The semiconducting P(NDI2DO-T2) material was spin-casted and dried with same condition for OFET samples.

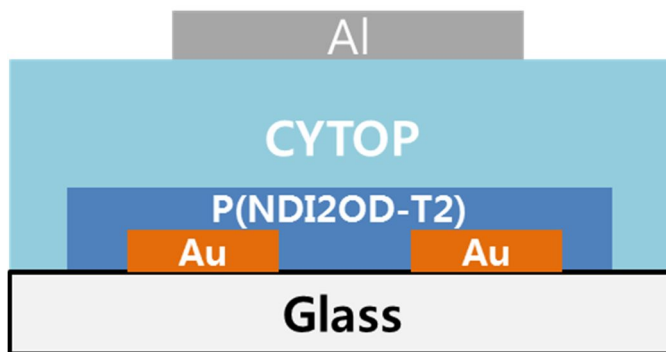


Figure 4.2 Schematic illustration of Bottom contact/Top gate OFET device with n-type dopants

4.3 Result and Discussion

4.3.1 FET characteristics of doped polymer

The OFET characteristics shown in Figure 4.3 (a) is n-channel operated (at the Source-Drain bias, $V_D = 20$ V and 80 V) transfer curve (I_D vs. V_G). Electron mobility and threshold voltage of this device is $0.38 \text{ cm}^2/\text{V}\cdot\text{sec}$ and $V_{TH} = 33.5$ V, respectively. I can confirm that P(NDI2OD-T2) is a well-known n-type semiconducting polymer but it also exhibit ambipolar characteristics with a low hole mobility as previously reported.³⁰ At the high source-drain bias, $V_D = 80$ V, the ambipolar current increased than at low source-drain bias, $V_D = 20$ V, in low low-gate voltage region. It is due to effective gate voltage of electron depends on applied source-drain bias. These n-type dominant ambipolar OFET characteristics are also shown in output curve (I_D vs. V_D) of OFET devices, Figure 4.3 (b). The hole mobility of this device was $8 \times 10^{-3} \text{ cm}^2/\text{V}\cdot\text{sec}$, more than one order than electron mobility. The transfer characteristics and output characteristics of p-type driving is shown in Figure 4.4.

The n-type transfer characteristics of OFET devices with various concentrations of C₆₀ and CsF doped P(NDI2OD-T2)

semiconducting layer are shown in Figure 4.5 (a) and (b), respectively. The P(NDI2OD-T2) reference FET device without any doping had mobility of $0.34 \text{ cm}^2/\text{V}\cdot\text{sec}$ and threshold voltage of -31.5 V . As increasing of C_{ocp2} doping ratio, the mobility was increased to $0.67 \text{ cm}^2/\text{V}\cdot\text{sec}$ at 0.25 wt% doping and $0.72 \text{ cm}^2/\text{V}\cdot\text{sec}$ at 0.50 wt%, respectively. However, the mobility of devices decreased when additional C_{ocp2} dopant is doped into the P(NDI2OD-T2) films. Similarly, the threshold voltages of OFET devices decreased gradually as the C_{ocp2} concentration increase and reached a minimum value, 8.8 V at 1.00 wt% of C_{ocp2}, and re-increased to 13.6 V at 2.00 wt% of C_{ocp2}. The subthreshold slope of C_{ocp2} doped OFET devices showed same tendency to threshold voltage. Interestingly, the CsF doped P(NDI2OD-T2) OFET devices showed different results. The output characteristics with 0.5wt% concentration of C_{ocp2} and CsF doped P(NDI2OD-T2) semiconducting layer are shown in Figure 4.6. The contact resistance decreased by doping compared to Figure 4.3 (b). The tendency of decreasing threshold voltage as doping concentration is same to C_{ocp2} doped devices. But the mobilities of CsF doped devices are not changed in error range as doping concentration less than 1.00 wt%. This result is summarized in Table 4.1 and Figure 4.7

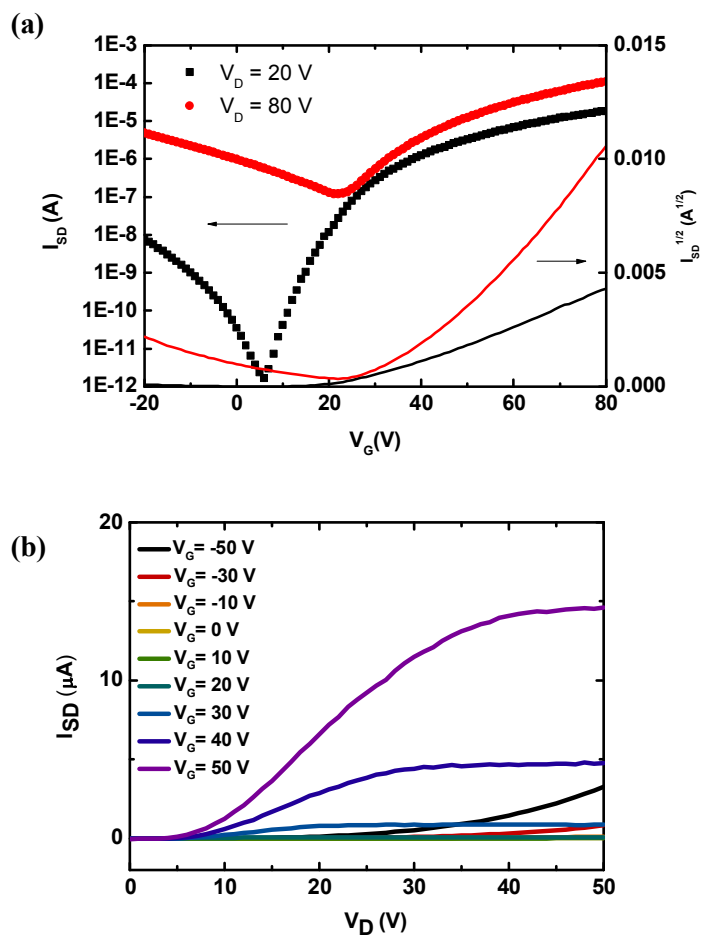


Figure 4.3 (a) The transfer characteristics of P(NDI2OD-T2) OFET in $V_D = 20 \text{ V}$, 80 V (b) Output characteristics of P(NDI2OD-T2) OFET with n-type operation

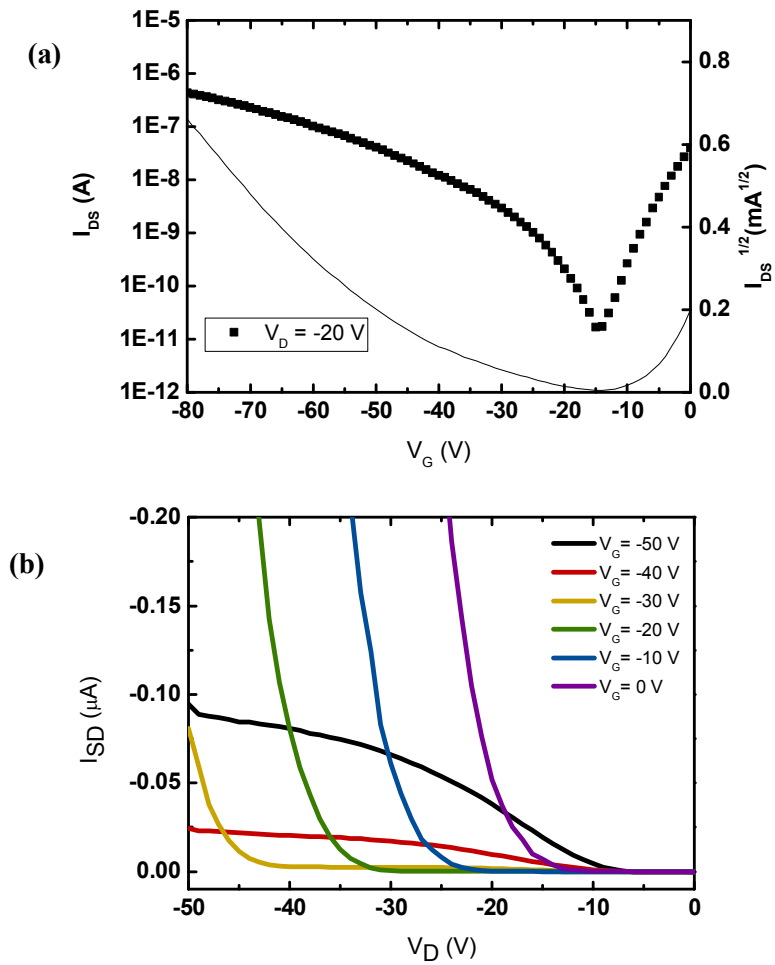


Figure 4.4 (a) Transfer characteristics of P(NDI2DO-T2) OFET with p-channel operation ($V_D = -20$ V) (b) Output characteristics of P(NDI2DO-T2) OFET with p-channel operation

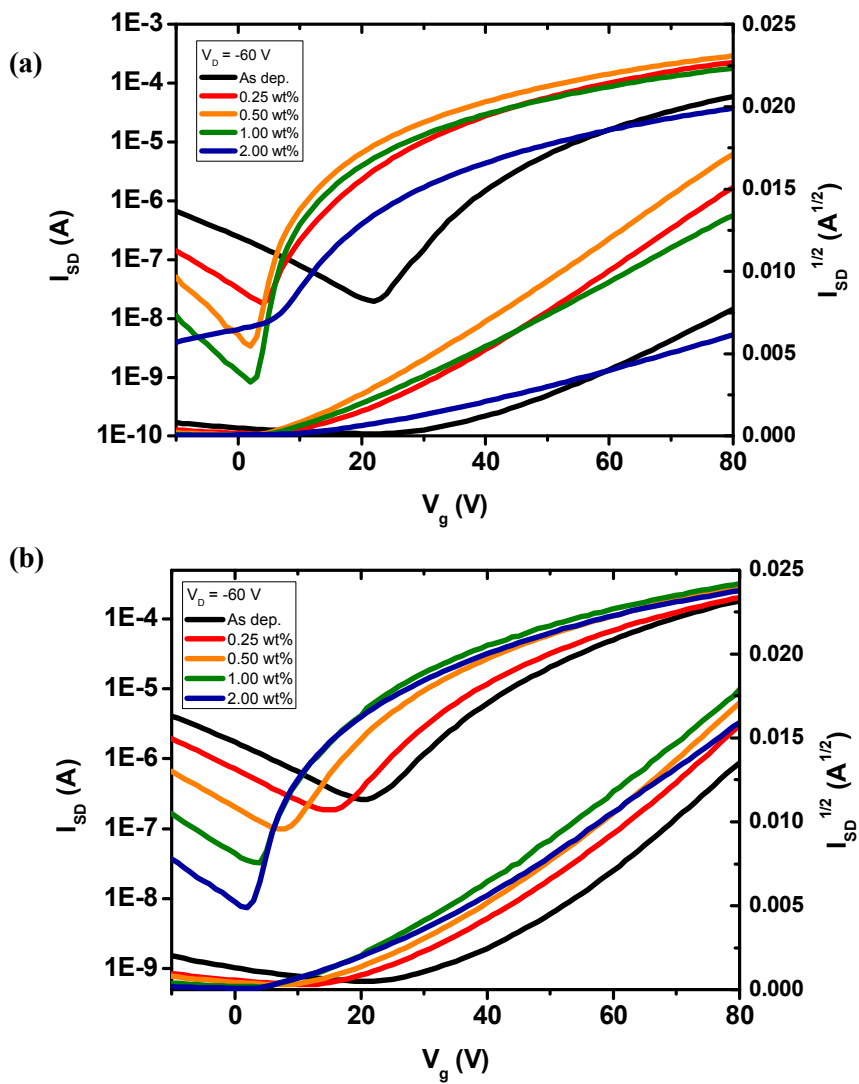


Figure 4.5 (a) The transfer characteristics of OFETs with various amount of (a) Cocp₂ and (b) CsF doping to P(NDI2OD-T2) semiconducting layer.

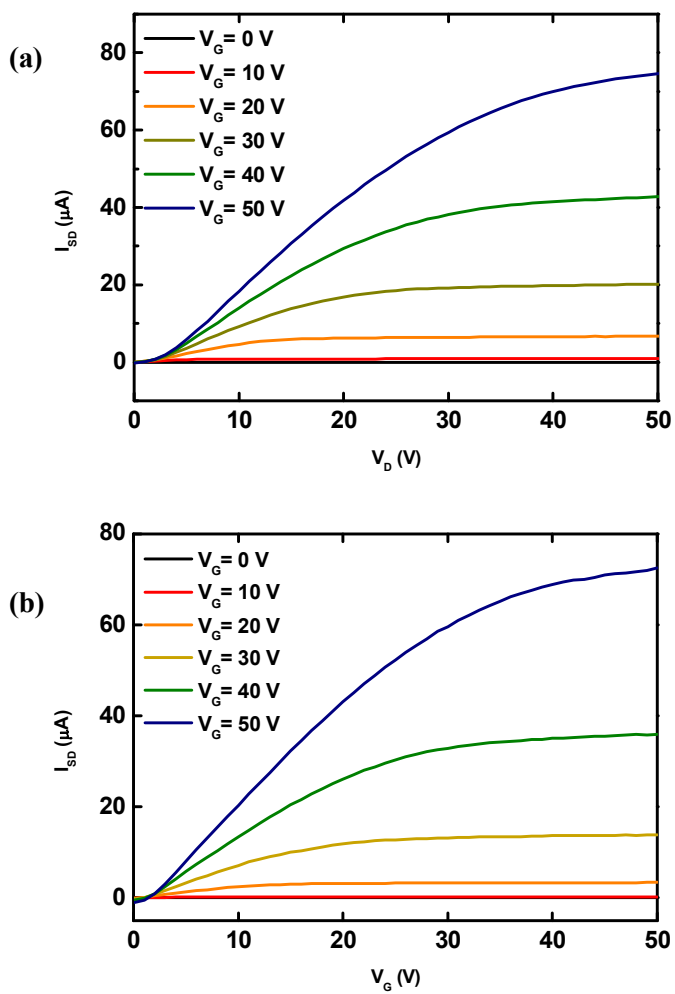


Figure 4.6 Output characteristics of P(NDI2DO-T2) OFET with (a) Cocp₂ 0.5 wt% doping (b) CsF 0.5 wt% doping

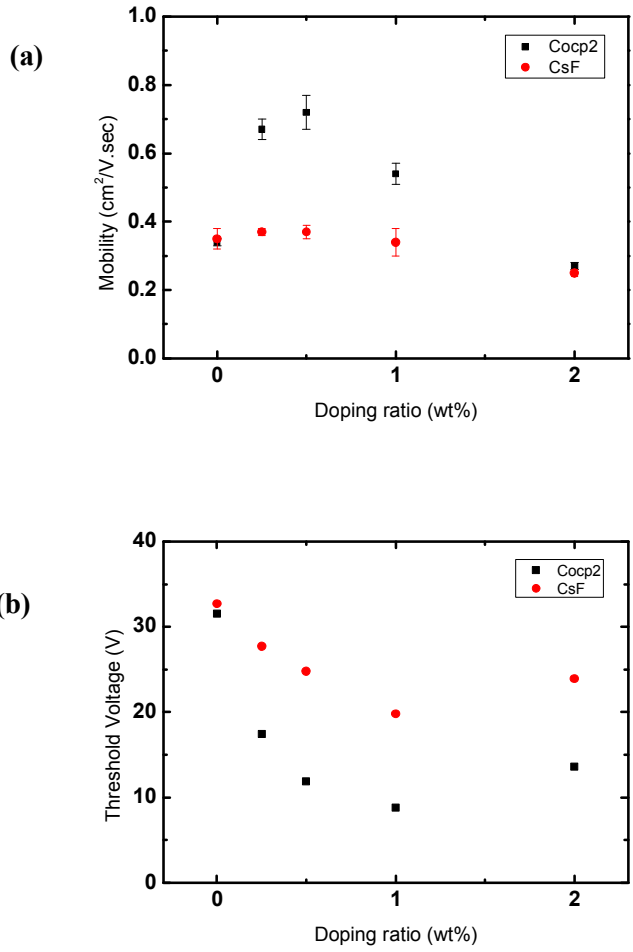


Figure 4.7 (a) The mobility change with various amount of n-type doping (b) The threshold voltage change with various amount of n-type doping

Doping concentration [wt %]	Cocp ₂ dopant			CsF dopant		
	Mobility [cm ² /V•sec]	V _{TH} [V]	S.S	Mobility [cm ² /V•sec]	V _{TH} [V]	S.S
As dep	0.34±0.01	31.5	8.6	0.35±0.03	32.7	11.3
0.25	0.67±0.03	17.4	5.3	0.37±0.01	27.7	8.3
0.50	0.72±0.05	11.9	3.2	0.37±0.02	24.8	8.0
1.00	0.54±0.031	8.8	7.9	0.34±0.04	19.8	5.2
2.00	0.27±0.01	13.6	9.2	0.25±0.01	23.9	4.4

Table 4.1 Summary of electrical property of OFET based on the pristine P(NDI2OD-T2) with different doping ratio

4.3.2 Stability of electrical parameter

Figure 4.8 shows the operational stability of the doped P(NDI2OD-T2) OFET devices under the cyclic bias stress. The 0.5 wt% concentration of C₆₀ and CsF were selected to maximize the effect of doping. I repeated 1000 times of sweep from $V_G = 0$ V to $V_G = 60$ V in $V_D = 40$ V and collected the data at the interval of each 50th scan. Because the P(NDI2OD-T2) material is stable in N₂ atmospheric condition, I assumed the changing of electrical characteristics is only affected by bias stress. Figure 4.8 (a) is the transfer characteristic change of OFET device without any doping. The red line is transfer characteristic of first scanning and the transfer curves are changed toward upside as measurement repeated. The FET mobility after 1000 cycles stressed device was about 70% increased at no-doped device. Figure 4.8 (b) and (c) is the transfer characteristic change of OFET devices with 0.5 wt% C₆₀ doping and 0.5 wt% CsF doping, respectively. These two devices after 1000 cycles stressed showed similar characteristics to first scanning. Figure 4.9 is summarization of mobility change and threshold voltage shift with bias stress cycles as dopant kind. According to the relationship in Equation 3, where q is

the elementary charge and C_{ox} is the capacitance of the gate dielectric per unit area, the V_{TH} shift can be converted to the trapped charge density, N_T .^{31, 32}

$$\Delta N_T = |\Delta V_{TH}| \frac{C_{ox}}{q} \quad (3)$$

The generated trap density of pristine, Cocup₂ doped and CsF doped P(NDI2OD-T2) after 1000 times cyclic bias are $2.3 \times 10^{12} \text{ cm}^{-3}$, $2.4 \times 10^{11} \text{ cm}^{-3}$ and $6 \times 10^{11} \text{ cm}^{-3}$, respectively. The free electrons generated by strong electron donating Cocup₂ or CsF can transfer to semiconducting layer and prevent generation of trap sites. However, in our system, generated traps increase source-drain current and mobility as result of positive bias stress and the reason is under investigated.

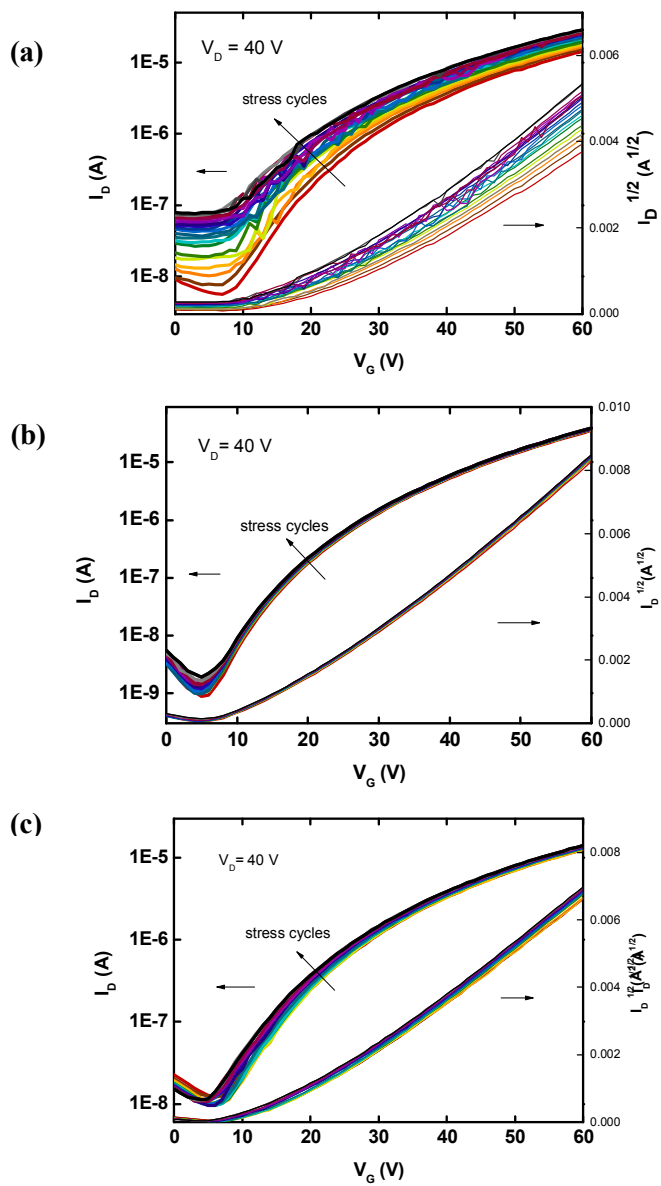


Figure 4.8 A change of transfer characteristics after bias stress test with (a) pristine (b) Cocl_2 doped (c) CsF doped devices.

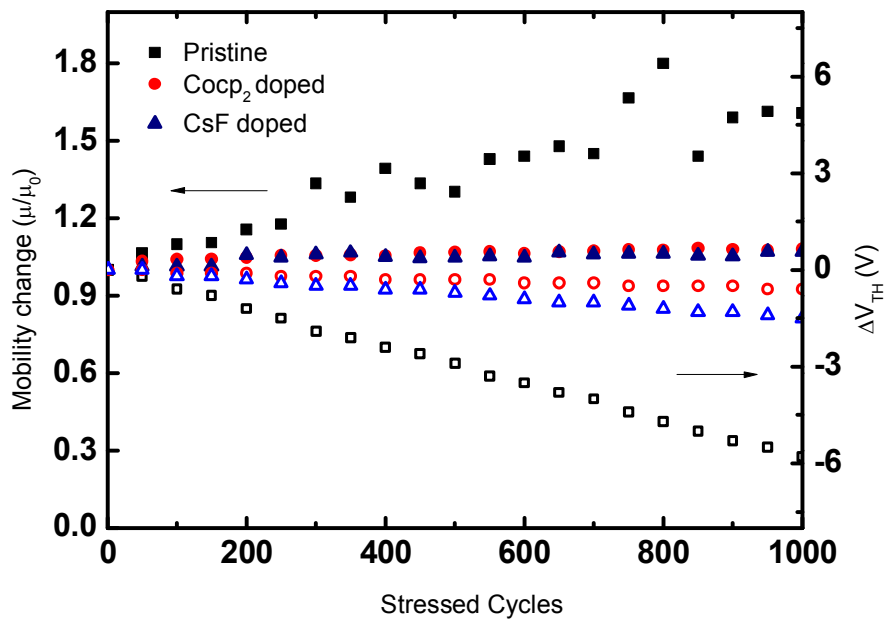


Figure 4.9 The mobility change and threshold voltage shift with stress cycles

4.3.3 Crystallinity analysis with X-ray scattering

In order to find out the origin of increased mobility of the C₆₀-doped P(NDI2OD-T2) OFET devices, the doped P(NDI2OD-T2) films were examined by Grazing Incidence X-Ray Diffraction (GIXRD) both the in-plane and out-of-plane direction. Atomic force microscope was also used to get topographic image of P(NDI2OD-T2) films, but failed to get significant crystal structure and only observed amorphous surface in the range of resolution of AFM. The out-of-plane XRD patterns of P(NDI2OD-T2) films showed only weak and broad peak at $q_z = 1.60 \text{ \AA}^{-1}$, same results as previously reported.²⁷ Figure 4.10 (a) and (b) are in-plane XRD patterns of C₆₀-doped and CsF-doped P(NDI2OD-T2) films, respectively, near the first peak position (100) at $q_{xy} = 0.25 \text{ \AA}^{-1}$. Both XRD patterns showed the same tendency that the intensity of the peak increased as the doping concentration increased to 0.50 wt%. However, the peak intensity of 1.00 wt% and 2.00 wt% doped films decreased compared to 0.50 wt%. It is reported that the P(NDI2OD-T2) film has a face-on molecular packing structure and the predominant (100) peak corresponds to the lamellar stacking peak. The increasing

intensity of this peak is due to the formation of charge complexes between electron-deficient polymer and electron-rich dopant. In contrast to well-ordered edge-on packed polymers, such as poly(3-hexyl thiophene, P3HT), increase of FET mobility could be expected as increasing the order of lamellar stacking in face-on packed polymer because charge carriers can escape a transport barrier near the dielectric interface by hopping to subsequent layers coupled by π -stacking out-of-plane.³³ Figure 4.11 (a) is in-plane XRD patterns of P(NDI2OD-T2) film (black line) , pure CsF film (blue line) and pure Cosp₂ film (red line). The out-of-plane x-ray diffraction patterns of the pristine P(NDI2OD-T2) , Cosp₂ and CsF film was shown in Figure 4.11 (b). These XRD patterns showed highly crystalline CsF can be act as impurity in manner of structural disorder. I suppose this is the reason why only Cosp₂ doping can increase FET mobility but more investigation is required.

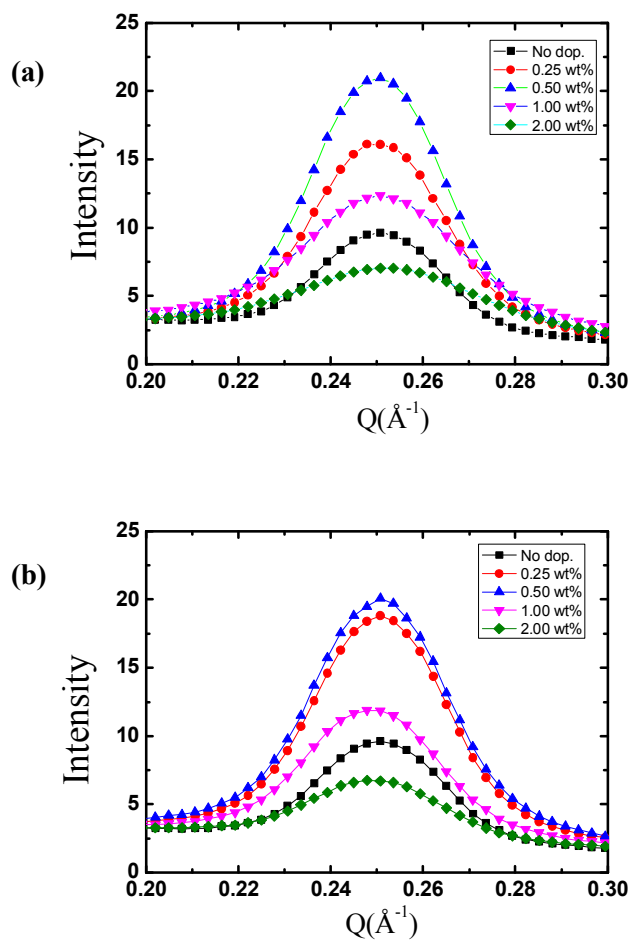


Figure 4.10 The in-plane x-ray diffraction patterns of the (a) P(NDI2OD-T2) with Cosp₂ dopant (b) P(NDI2OD-T2) with CsF dopant

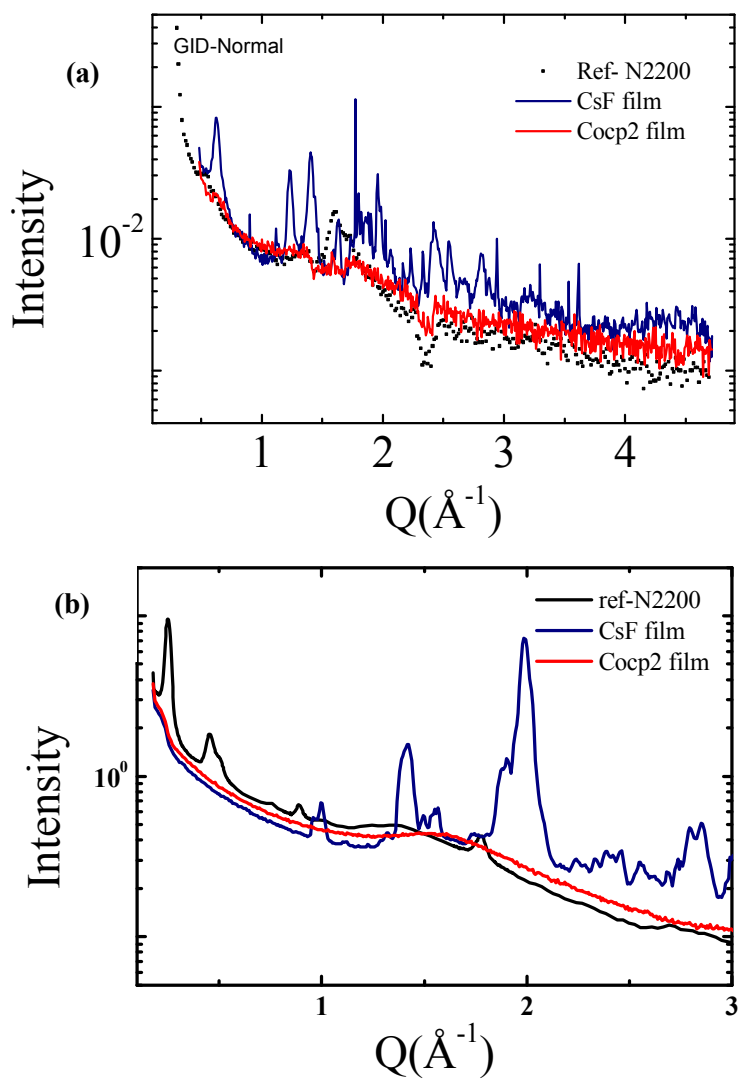


Figure 4.11 (a) The in-plane and (b) The out-of-plane x-ray diffraction patterns of pristine P(NDI2OD-T2) , Cocp₂ and CsF film with wide range

4.4 Conclusion

I have fabricated the P(NDI2OD-T2) OFETs with various concentration of the electron donor C₆₀ and CsF. The field-mobility mobility of CsF doped P(NDI2OD-T2) OFET devices are not affected by doping concentration. But the field-mobility and the bias stress resistance of C₆₀ doped P(NDI2OD-T2) OFET devices are increased and threshold voltage is decreased than that of the device without doping. And I found out reducing of contact resistance and ambient leakage current by doping. I want to investigate that reason from microstructure analysis with synchrotron X-ray diffraction geometries. Charge-transfer complexes between dopant molecule and host polymer lead to an increasing of lamellar packing that can contribute to transporting of charge carrier in face-on molecular arrangement. These results could be applied to another n-type polymer with similar face-on microstructure.

4.5 Bibliography

1. H. Chen, Y. Guo, G. Yu, Y. Zhao, J. Zhang, D. Gao, H. Liu, Y. Liu, *Advanced Materials* **24**,4618 (2012)
2. Z. Chen, M. J. Lee, R. Shahid Ashraf, Y. Gu, S. Albert-Seifried, M. Meedom Nielsen, B. Schroeder, T. D. Anthopoulos, M. Heeney, I. McCulloch, H. Sirringhaus, *Advanced Materials* **24**,647 (2012)
3. J. S. Lee, S. K. Son, S. Song, H. Kim, D. R. Lee, K. Kim, M. J. Ko, D. H. Choi, B. Kim, J. H. Cho, *Chemistry of Materials* **24**,1316 (2012)
4. H.-W. Lin, W.-Y. Lee, W.-C. Chen, *Journal of Materials Chemistry* **22**,2120 (2012)
5. C. B. Nielsen, M. Turbiez, I. McCulloch, *Advanced Materials* **25**,1859 (2013)
6. J. D. Yuen, J. Fan, J. Seifter, B. Lim, R. Hufschmid, A. J. Heeger, F. Wudl, *Journal of the American Chemical Society* **133**,20799 (2011)
7. H. T. Nicolai, M. Kuik, G. A. H. Wetzelaer, B. de Boer, C. Campbell, C. Risko, J. L. Brédas, P. W. M. Blom, *Nat Mater* **11**,882 (2012)
8. J. A. Letizia, M. R. Salata, C. M. Tribout, A. Facchetti, M. A.

- Ratner, T. J. Marks, *Journal of the American Chemical Society* **130**,9679 (2008)
9. X. Zhan, Z. a. Tan, B. Domercq, Z. An, X. Zhang, S. Barlow, Y. Li, D. Zhu, B. Kippelen, S. R. Marder, *Journal of the American Chemical Society* **129**,7246 (2007)
 10. S. Huttner, M. Sommer, M. Thelakkat, *Applied Physics Letters* **92**,093302 (2008)
 11. H. Yan, Z. Chen, Y. Zheng, C. Newman, J. R. Quinn, F. Dotz, M. Kastler, A. Facchetti, *Nature* **457**,679 (2009)
 12. M. Caironi, M. Bird, D. Fazzi, Z. Chen, R. Di Pietro, C. Newman, A. Facchetti, H. Sirringhaus, *Advanced Functional Materials* **21**,3371 (2011)
 13. G.-J. A. H. Wetzelaer, M. Kuik, Y. Olivier, V. Lemaure, J. Cornil, S. Fabiano, M. A. Loi, P. W. M. Blom, *Physical Review B* **86** (2012)
 14. R. Kim, P. S. K. Amegadze, I. Kang, H.-J. Yun, Y.-Y. Noh, S.-K. Kwon, Y.-H. Kim, *Advanced Functional Materials*, n/a (2013)
 15. K. Walzer, B. Maennig, M. Pfeiffer, K. Leo, *Chemical Reviews* **107**,1233 (2007)
 16. D.-S. Leem, H.-D. Park, J.-W. Kang, J.-H. Lee, J. W. Kim, J.-J. Kim, *Applied Physics Letters* **91**,011113 (2007)

17. J.-H. Lee, D.-S. Leem, H.-J. Kim, J.-J. Kim, *Applied Physics Letters* **94**,123306 (2009)
18. Y. Zhang, B. de Boer, P. W. M. Blom, *Physical Review B* **81**,085201 (2010)
19. S. Olthof, S. Mehraeen, S. K. Mohapatra, S. Barlow, V. Coropceanu, J.-L. Brédas, S. R. Marder, A. Kahn, *Physical Review Letters* **109**,176601 (2012)
20. P. Wei, J. H. Oh, G. Dong, Z. Bao, *Journal of the American Chemical Society* **132**,8852 (2010)
21. C. Y. H. Chan, C. M. Chow, S. K. So, *Organic Electronics* **12**,1454 (2011)
22. J. S. Swensen, L. Wang, J. E. Rainbolt, P. K. Koech, E. Polikarpov, D. J. Gaspar, A. B. Padmaperuma, *Organic Electronics* **13**,3085 (2012)
23. L. Ma, W. H. Lee, Y. D. Park, J. S. Kim, H. S. Lee, K. Cho, *Applied Physics Letters* **92**,063310 (2008)
24. J. H. Kim, S. W. Yun, B.-K. An, Y. D. Han, S.-J. Yoon, J. Joo, S. Y. Park, *Advanced Materials* **25**,719 (2013)
25. P. Wei, T. Menke, B. D. Naab, K. Leo, M. Riede, Z. Bao, *Journal of the American Chemical Society* **134**,3999 (2012)

26. J. H. Oh, P. Wei, Z. Bao, *Applied Physics Letters* **97**,243305 (2010)
27. J. Rivnay, M. F. Toney, Y. Zheng, I. V. Kauvar, Z. Chen, V. Wagner, A. Facchetti, A. Salleo, *Advanced Materials* **22**,4359 (2010)
28. C. K. Chan, F. Amy, Q. Zhang, S. Barlow, S. Marder, A. Kahn, *Chemical Physics Letters* **431**,67 (2006)
29. J. Jang, J. W. Kim, N. Park, J.-J. Kim, *Organic Electronics* **9**,481 (2008)
30. K.-J. Baeg, D. Khim, S.-W. Jung, M. Kang, I.-K. You, D.-Y. Kim, A. Facchetti, Y.-Y. Noh, *Advanced Materials* **24**,5433 (2012)
31. K. P. Pernstich, S. Haas, D. Oberhoff, C. Goldmann, D. J. Gundlach, B. Batlogg, A. N. Rashid, G. Schitter, *Journal of Applied Physics* **96**,6431 (2004)
32. J. A. Letizia, J. Rivnay, A. Facchetti, M. A. Ratner, T. J. Marks, *Advanced Functional Materials* **20**,50 (2010)
33. A. Salleo, *Materials Today* **10**,38 (2007)

초 록

동작 안정성은 유기 트랜지스터의 성능을 평가하는데 가장 중요한 요소 중의 하나이다. 동작 안정성을 평가하기 위해서 이 논문에서는 통제된 환경 내에서 게이트, 소스, 드레인 전극에 일정 시간 동안 연속 또는 교대전압을 인가하여 트랜지스터 특성을 시간에 따라 주기적으로 관찰하였다.

1장에서는 반도체와 트랜지스터의 작동 원리, 유기반도체의 종류와 응용 분야에 대해 소개하였다.

2장에서는, 불소계고분자를 절연막으로 이용하여 공기 중에서 안정한 전자 이동특성을 가진 C₆₀ 트랜지스터를 구현하였다. 기존에 사용하던 SiO₂ 절연체는 공기중에서 이 소자를 동작시키지 않는데 비해 이 소자는 공기 중에서 0.49 cm²/V·s의 전하이동도를 나타내었다. 이 불소고분자는 반도체와 절연체 사이의 계면에 형성된 트랩의 형성을 막았기 때문에 이런 결과를 얻을 수 있었다.

안정적인 유기 트랜지스터를 이용한 이온 및 바이오 센서에 대해서 3장에서 다루고 있다. 유기 트랜지스터의 안정성은 물 속에서 동작하기 때문에 센서 제작에 있어서 가장 중요한 요소이다. 양성자 이온 센서가 이온 검출이 가능한 절연막을 이용하여 제작되었다. 각기 다른 수소이온농도를 가진 용액에서 전류 특성 변화가 보이는 것을 분석하였다. 그리고 소 혈청 알부민이 개질된 표면에 공유결합시켜 소자가 이 물

질의 항체와 선택적으로 결합한 것을 감지할 수 있도록 한 바이오 센서를 제작하였다. 이 센서는 기존에 사용되던 광학적 원리의 센서보다 높은 반응상수를 가진 것으로 나타났다. 빠르고 실시간으로 라벨없이 높은 민감도를 구현한 유기 트랜지스터 바이오센서는 이온화가 가능한 그룹이 있는 다른 물질에게도 적용될 수 있으며 이를 통해 마이크로 어레이 센서를 만들 수 있을 것이다.

4장에서는 전자이동특성을 가진 P(NDI2OD-T2) 고분자에 도핑을 하여 도핑농도가 소자의 전기적 특성 및 안정성에 미치는 영향에 관한 내용을 다루었다. 높은 결정성을 가진 CsF가 도핑된 트랜지스터에서는 전하이동도의 차이를 보이지 않은 반면, 비정질의 C₆₀가 도핑된 트랜지스터에서는 전하이동도가 0.35 cm²/V•sec 에서 0.72 cm²/V•sec까지 증가하였다. 두 종류의 도펀트 모두 향상된 문턱전압 특성과 반복되는 구동에 대한 안정성이 향상되었다. 이러한 원인을 찾기 위해 X선 회절 분석이 진행되었다. 도펀트에 의해 생성된 전자에 의해 반도체 내의 트랩이 채워지고 결정성이 향상되어서 이러한 결과를 얻은 것으로 분석되었다.

주요어 : 유기반도체, 고분자반도체, 도핑, 유기트랜지스터, 바이오센서, 전하이동도, 안정성

학번 : 2004-23463

List of publications

1. **Junhyuk Jang**, Ji Whan Kim, Nohhwal Park, Jang-Joo Kim, “Air stable C₆₀ based n-type organic field effect transistor using a perfluoropolymer insulator”, *Organic Electronics*, **9** 481 (2008)
2. Myoung-Chul Um, **Junhyuk Jang**, Jihoon Kang, Jung-Pyo Hong, Do Yeung Yoon, Seong Hoon Lee, Jang-Joo Kim and Jong-In Hong, “High-performance organic semiconductors for thin-film transistors based on 2,6-bis(2-thienylvinyl)anthracene”, *Journal of Materials Chemistry*, **18**, 2234 (2008)
3. Myoung-Chul Um, **Junhyuk Jang**, Jung-Pyo Hong, Jihoon Kang, Do Yeung Yoon, Seong Hoon Lee, Jang-Joo Kim and Jong-In Hong, “Organic thin-film transistors based on 2,6-bis(2-arylvinyl)anthracene:high-performance organic semiconductors”, *New Journal of Chemistry*, **32**, 2006 (2008)
4. Hadayat Ullah Khan, **Junhyuk Jang**, Jang-Joo Kim, and Wolfgang Knoll, “In Situ Antibody Detection and Charge Discrimination Using Aqueous Stable Pentacene Transistor Biosensors”, *Journal of the American Chemical Society*, **133**, 2170 (2011)

5. Hadayat Ullah Khan, **Junhyuk Jang**, Jang-Joo Kim, Wolfgang Knoll, “Effect of passivation on the sensitivity and stability of pentacene transistor sensors in aqueous media”, *Biosensors and Bioelectronics* , **26** , 4217 (2011)
6. Hyo Jung Kim, Ji Whan Kim, Hyun Hwi Lee, Tae-Min Kim, **Junhyuk Jang**, and Jang-Joo Kim, "Grazing Incidence Small-Angle X-ray Scattering Analysis of Initial Growth of Planar Organic Molecules Affected by Substrate Surface Energy”, *The Journal of Physical Chemistry Letters*, **2**, 1710 (2011)
7. Sung-Hwan Choi, **Junhyuk Jang**, Jang-Joo Kim, and Min-Koo Han, “Low-Temperature Organic (CYTOP) Passivation for Improvement of Electric Characteristics and Reliability in IGZO TFTs”, *IEEE ELECTRON DEVICE LETTERS*, **33**, 381 (2012)